Available online at www.CivileJournal.org

Civil Engineering Journal

(E-ISSN: 2476-3055; ISSN: 2676-6957)

Vol. 11, No. 12, December, 2025

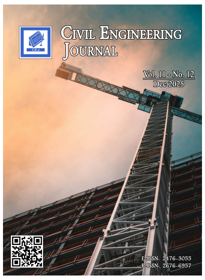

Robust Ensemble Machine Learning for Flash Flood Susceptibility Mapping Across Semiarid Regions

Soukaina Talha [1*], Ahmed Akhssas [1], Abdellatif Aarab [2], Ayoub Aabi [3], Badr Berkat [1], Said Amouch [1]

[1] *Laboratory of Applied Geophysics, Geotechnics, Engineering Geology, and Environment, Mohammadia Engineering School, Mohammed V University in Rabat, 765, Av. Ibn Sina, Agdal, Rabat, Morocco.*

[2] *Laboratory for Water Analysis and Modeling of Natural Resources, Mohammadia Engineering School, Mohammed V University in Rabat, BP:765 Ibn Sina Avenue Agdal, Rabat, Morocco.*

[3] *Department of Earth Sciences, École Normale Supérieure, Mohammed V University in Rabat, Morocco.*

Received 26 April 2025; Revised 11 November 2025; Accepted 18 November 2025; Published 01 December 2025

Abstract

Flash floods cause severe environmental and socio-economic impacts in arid and semi-arid regions. This study aims to improve the accuracy of flash flood susceptibility mapping in southwestern Morocco's Assaka watershed by using an ensemble of machine learning models. Four models, Logistic Regression (LR), Multivariate Discriminant Analysis (MDA), Naïve Bayes (NB), and Multilayer Perceptron (MLP), were trained on a flood inventory of over 1.5 million data points and 14 environmental factors (e.g., altitude, slope, land surface temperature, soil moisture index). Each model produced a susceptibility map, and a voting ensemble of the top-performing models (all above 80% accuracy) further improved reliability. The MLP achieved the highest predictive performance, followed closely by LR and MDA. Sensitivity analysis identified altitude, topographic position index, land surface temperature, and soil moisture index as the most influential factors. The ensemble susceptibility map highlights densely populated areas near the city of Guelmim and infrastructure along major rivers as most prone to flash flooding. These findings enable practical mitigation measures such as improved drainage, early warning systems, and better land-use planning in high-risk zones. Integrating multiple models in an ensemble is a novel approach that reduces uncertainty and provides a more robust tool for flash flood risk prediction.

Keywords: Flash Flood; Ensemble Modeling; Machine Learning; GIS; FAHP; Susceptibility Mapping; Environmental Risk; Spatial Analysis.

---

1. Introduction

Flash floods are globally recognized as among the most destructive natural disasters, and their severity is escalating due to climate change, rapid urbanization, and land-use alterations. These sudden flood events cause profound ecological disruption, infrastructure damage, agricultural losses, and tragic human fatalities [1]. In Morocco, floods account for about 70% of officially recognized natural disasters [2]. The semi-arid Guelmim-Oued Noun region in southern Morocco has experienced recurrent catastrophic flash floods, notably in 1968, 1985, 1989, 2002, 2010, and most severely in 2014 (Figures 1 and 2) [3]. The 2014 event alone killed at least 32 people (including 24 in the Guelmim area) and left several missing [3], while destroying around 100 mud-brick homes and cutting off 100+ roads (including major highways) in the region [1]. This devastation underscored the urgent need for improved flash flood prediction and risk reduction strategies in the region.

---

* Corresponding author: soukaina_talha2@um5.ac.ma

http://dx.doi.org/10.28991/CEJ-2025-011-12-02

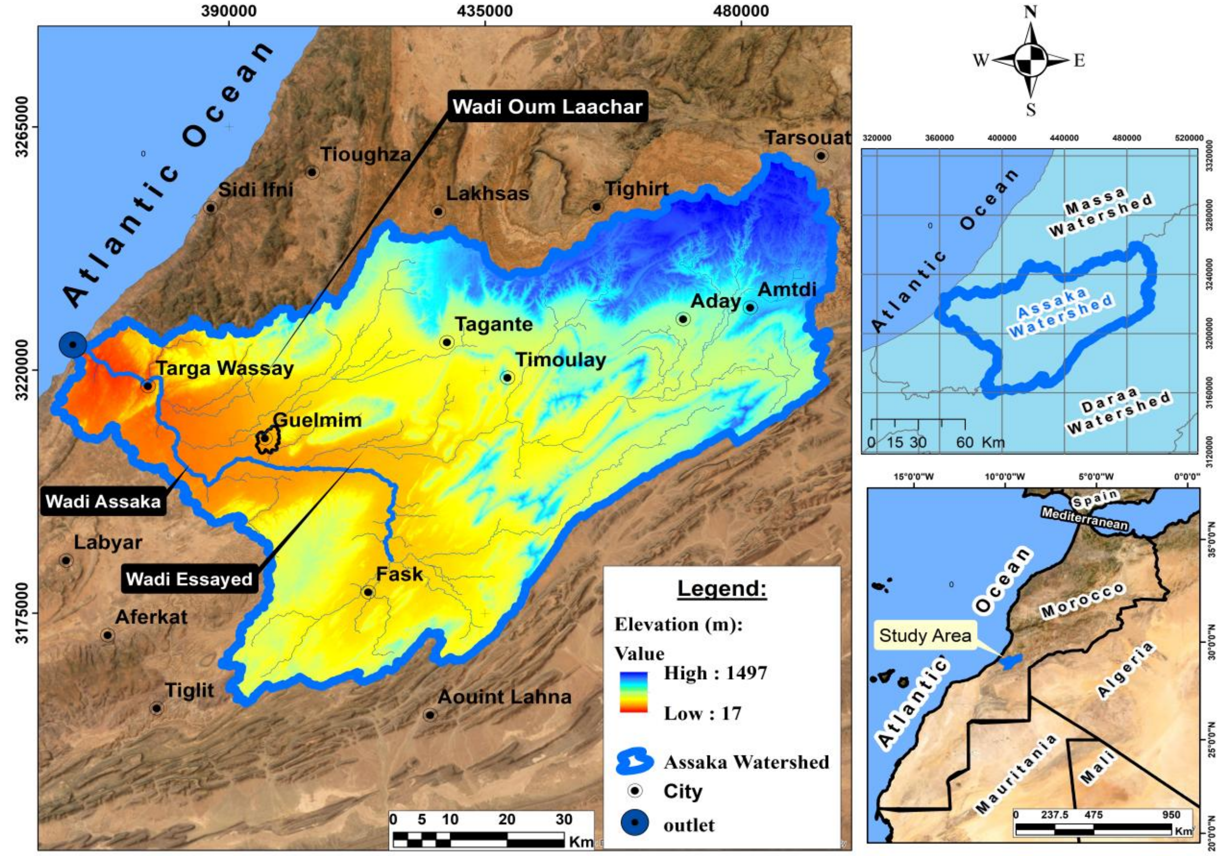

Figure 1. Geographical overview of the ASSAKA watershed area

Figure 2. Effects of flooding within the ASSAKA watershed (23 November 2014) (Said Amouch)

The Assaka watershed, the focus of this study, is one of the largest and most flood-prone basins in southwestern Morocco. Covering approximately 6,862 km² with terrain ranging from Atlantic coastal plains to mountains over 1,100 m high, the watershed features complex geomorphology and steep gradients that accelerate runoff. The climate is arid to semi-arid with sparse, erratic rainfall averaging ~145 mm annually [2]. Wide alluvial valleys and flat depressions (300–600 m elevation) dominate the landscape, but soils of predominantly low permeability (e.g., clay-rich siltstones and shales) severely limit infiltration. Consequently, intense rainstorms generate rapid surface runoff and overflow, causing frequent flash flooding. Historically, these floods have repeatedly impacted communities. For example, Guelmim city was officially declared a disaster zone after the 2014 floods due to extensive infrastructure destruction and loss of life [3]. Such events highlight the need for precise, data-driven flood susceptibility mapping to support early warnings and land-use planning.

Traditionally, flood susceptibility in regions like Assaka has been assessed using Geographic Information System (GIS) analyses combined with expert-based multi-criteria methods. For instance, analytical hierarchy process (AHP) and fuzzy logic approaches have been applied to integrate various flood factors with expert judgment [4]. Khaddari et al. (2023) [4] produced flood susceptibility maps for the Assaka watershed using a Fuzzy-AHP method, achieving an accuracy around 89–90% (AUC) [4]. While such GIS-based techniques are useful, they inherently rely on subjective weighting of factors, introducing uncertainty and potential bias. In recent years, data-driven machine learning (ML) models have gained traction for flood risk mappin [5]. Supervised ML algorithms like logistic regression, decision trees, random forests, support vector machines, and neural networks can objectively learn complex relationships from historical flood data and environmental predictors. Several studies have demonstrated the promise of ML in improving flood prediction accuracy [5]. For example, Razali et al. (2020) [6] and El-Haddad et al. (2021) [7] applied algorithms such as Naïve Bayes (NB), Logistic Regression (LR), Multivariate Discriminant Analysis (MDA), and Artificial Neural Networks (ANN) to model flood-prone areas, yielding better objectivity than expert scoring methods. However, standalone ML models also have limitations; each algorithm has different predictive biases and may perform inconsistently under varying conditions. Individual models can be sensitive to training data idiosyncrasies, suffer generalization issues, or provide limited interpretability of physical flood driver [5].

To address these gaps, this study proposes a novel ensemble machine learning framework for flash flood susceptibility mapping in the Assaka watershed. Ensemble learning theory suggests that combining multiple diverse models can reduce individual errors and yield more robust predictions. By integrating the outputs of several high-performing classifiers, the ensemble approach can capitalize on their complementary strengths while mitigating weaknesses of any single model [5]. In this research, we develop an ensemble voting model that merges four algorithms, LR, MDA, NB, and a multi-layer perceptron (MLP) neural network, to improve flash flood susceptibility estimation. These particular algorithms were chosen based on preliminary tests indicating each achieved over 80% predictive accuracy individually, ensuring that only strong learners contribute to the final ensemble. The theoretical premise is that their combination will provide a more reliable and generalized tool for spatial flood risk prediction than any stand-alone model [5]. This approach is relatively new in the context of Moroccan watersheds; to our knowledge, no prior study in Morocco's semi-arid regions has integrated multiple ML models into an ensemble for flood mapping. Singha et al. (2022) [8], for example, applied single ML algorithms to map flood zones in the Ourika watershed, but did not explore an ensemble strategy.

Our objectives are (1) to improve flash flood susceptibility mapping accuracy through an ensemble of ML models, (2) to quantify the influence of various environmental factors (altitude, slope, land use, soil moisture, lithology, etc.) on flood occurrence, and (3) to pinpoint the most vulnerable areas within the Assaka watershed for targeted risk mitigation. By analyzing model outputs and conducting sensitivity tests (e.g., Jackknife analysis), we identify which conditioning factors most strongly control flash flood potential in this basin. The central hypothesis is that the ensemble model will outperform the individual classifiers in predictive capability, thereby providing a more robust and trustworthy flood susceptibility map. This integrated modeling approach is expected to reduce the uncertainty associated with any one method and yield clearer insights into flash flood dynamics. In doing so, the study fills a key knowledge gap regarding effective ensemble flood modeling in semi-arid environments. The resulting susceptibility map highlights priority zones (e.g., densely populated lowlands around Guelmim and infrastructure along Wadi Essayed and Oum Laachar) that are most prone to flash flooding. These findings can directly inform practical measures such as engineered drainage improvements, community early-warning systems, and land-use planning policies to minimize future flood damage.

The remainder of this article is organized as follows. Section 2 describes the study area and outlines the data and methodology, including the preparation of a flash flood inventory and the development of the four ML models and their ensemble integration. Section 3 presents the results and discussion, comparing the performance of individual models and the ensemble, analyzing the spatial patterns of flood susceptibility, and examining the importance of each predictor variable (with a theoretical discussion of the ensemble's advantages). Section 4 concludes the paper with key findings, practical recommendations for flood risk management, and suggestions for future research.

2. Materials and Methods

2.1. The Study Area

In southern Morocco, the Assaka watershed lies within the Guelmim-Oued Noun administrative region and is managed by the Souss Massa Hydraulic Basin Agency (ABHSM). It encompasses roughly 6,862 km², with a perimeter of about 597 km. The landscape is diverse, transitioning from Atlantic coastal plains to rugged mountains in the northeast, with elevations ranging from sea level along the coast to over 1,100 m in the highlands. The climate is arid to semi-arid desert, characterized by an average annual temperature of ~19°C and low, irregular precipitation on the order of 145 mm per year [9].

As of the 2014 census, the Assaka watershed's population was on the order of tens of thousands (exceeding 18,000 inhabitants). This population has been steadily increasing in recent decades, contributing to accelerated urban expansion and agricultural development in the region. For example, the city of Guelmim (the regional capital) grew from roughly 95,700 residents in 2004 to about 118,300 in 2014 [10]. By 2024, Guelmim's population reached approximately 126,700, underscoring the consistent demographic growth in the area [11]. Such growth has expanded urban and farming areas, thereby increasing the region's vulnerability to flooding.

Historically, the Assaka watershed has experienced multiple major floods, notably in 1968, 1985, 1989, 2002, and 2010, with the most catastrophic events occurring in late 2014. In that November 2014 flood, torrential rains generated severe flash floods that devastated the Guelmim area: at least 24 people were killed near the city of Guelmim alone [12], and the destruction of infrastructure (roads, bridges, homes, etc.) was so widespread that authorities officially declared the Guelmim region a disaster area [13]. These floods caused profound socio-economic disruptions and highlighted the urgent need for improved flood management.

Hydrologically, the Assaka watershed is drained by two main rivers, Oum Laachar and Essayed (also spelled El Sayed), which converge before flowing into the Atlantic Ocean. The terrain includes broad valleys and extensive depressions with flat bottoms primarily at 300–600 m elevation [9]. Gently sloping plateaus around 350–400 m, interspersed with sharper topographical gradients, strongly influence how water runs off and accumulates. The basin's slope generally decreases from northeast to southwest, resulting in large areas with moderate slopes (under ~11°) [9]. Morphometric analyses have noted that the wide valleys and tableland regions with gentle grades serve as natural flow pathways, affecting flood patterns in the region.

Overall, flood susceptibility in the Assaka watershed is exacerbated by a combination of factors: steep upstream gradients, insufficient drainage infrastructure, and soils with low permeability that hinder the absorption of heavy rainfall. As a result, intense rain events can rapidly produce flash floods along rivers like Oum Laachar and Essayed, frequently causing severe damage to roads, bridges, dwellings, and agricultural lands in their path. Such recurring flood events pose significant long-term risks to local economic stability and livelihoods, underscoring the need for precise, detailed flood risk assessments to inform better preparedness and mitigation planning in the future.

2.2. Methodology

The methodology employed in this study is summarized in the flowchart shown in Figure 3. The main steps include: (a) exporting a flash flood target map, (b) preprocessing the conditioning factors, (c) predicting flash flood susceptibility using MDA, LR, NB, and MLP algorithms, (d) assessing model performance (accuracy threshold ≥ 80%), (e) generating susceptibility maps, and (f) producing a composite ensemble map.

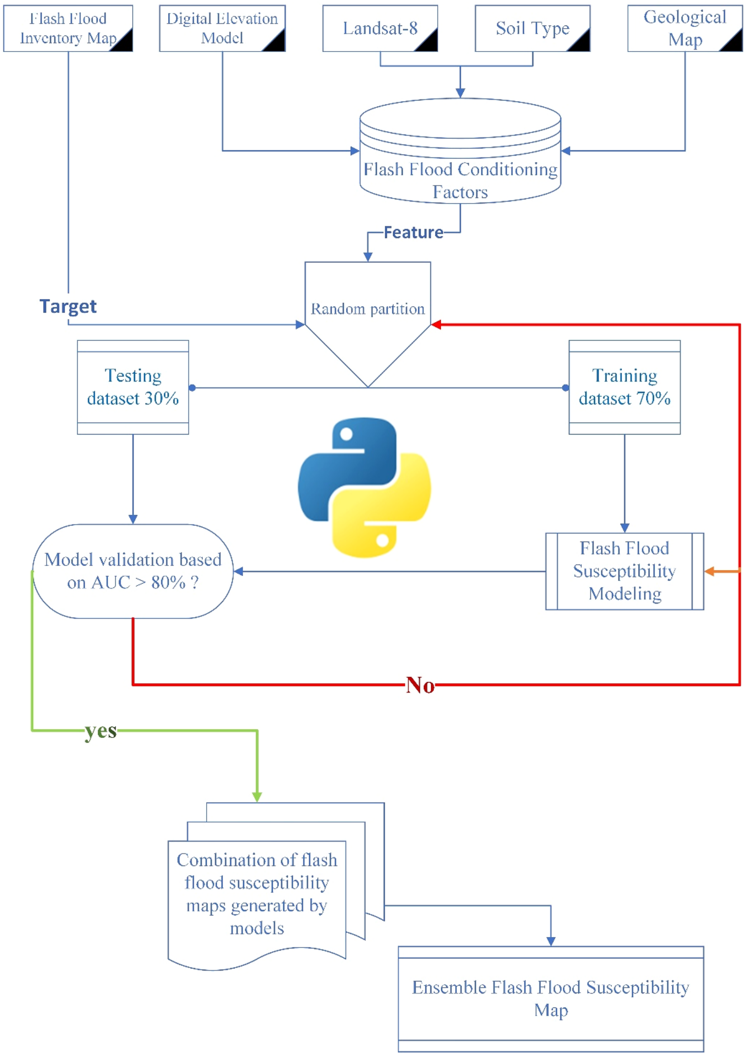

Figure 3. Prediction of sudden flood risk applying MDA, LR, NB, and MLP algorithms

2.2.1. Flash Flood Target Map

A binary flood-inventory (target) was derived from the FAHP susceptibility map of the study by Talha et al. (2019) [14] (Figure 4-o). The Assaka watershed (≈6,800 km²) was rasterized to the analysis grid, yielding >8 million spatial samples (cells) (Figure 4-o). Cells in the FAHP High and Highest classes were coded as flood-prone (positive); all others were coded as non-flood (negative). This procedure produced 1,514,434 positive cells, with the remaining cells forming the negative class. The complete labeled grid was used for model development. The dataset was randomly partitioned into training (70%) and testing (30%) subsets using train_test_split (without replacement, class proportions preserved) to ensure unbiased evaluation.

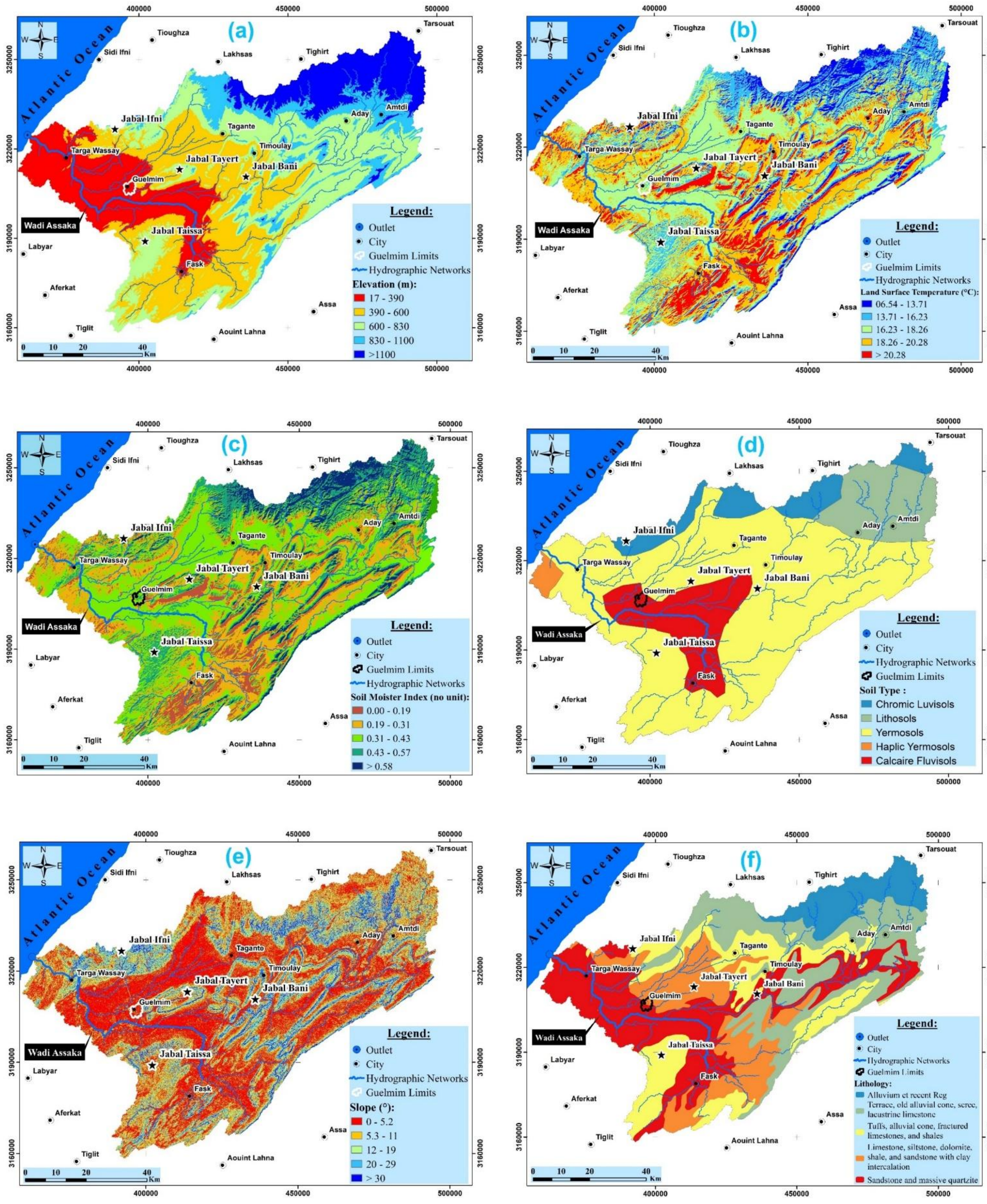

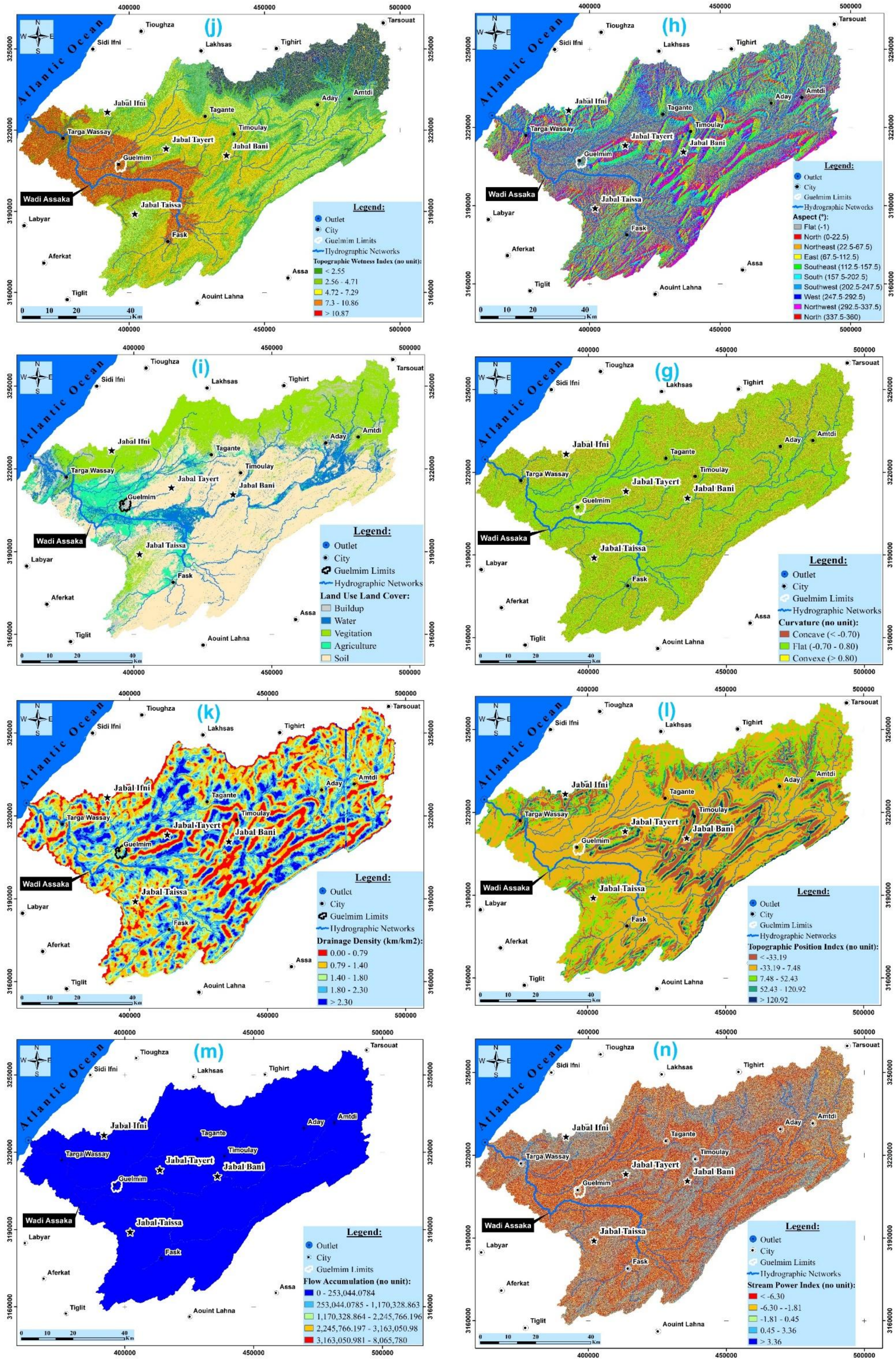
(j)
Atlantic Ocean
Wadi Assaka
Legend:
Outlet
City
Guelmim Limits
Hydrographic Networks
Topographic Wetness Index (no unit):
< 2.55
2.56 - 4.71
4.72 - 7.29
7.3 - 10.86
> 10.87
(h)
Legend:
Outlet
City
Guelmim Limits
Hydrographic Networks
Aspect (°):
Flat (-1)
North (0-22.5)
Northeast (22.5-67.5)
East (67.5-112.5)
Southeast (112.5-157.5)
South (157.5-202.5)
Southwest (202.5-247.5)
West (247.5-292.5)
Northwest (292.5-337.5)
North (337.5-360)
(i)
Legend:
Outlet
City
Guelmim Limits
Hydrographic Networks
Land Use Land Cover:
Buildup
Water
Vigitation
Agriculture
Soil
(g)
Legend:
Outlet
City
Guelmim Limits
Hydrographic Networks
Curvature (no unit):
Concave (< -0.70)
Flat (-0.70 - 0.80)
Convexe (> 0.80)
(k)
Legend:
Outlet
City
Guelmim Limits
Hydrographic Networks
Drainage Density (km/km2):
0.00 - 0.79
0.79 - 1.40
1.40 - 1.80
1.80 - 2.30
> 2.30
(l)
Legend:
Outlet
City
Guelmim Limits
Hydrographic Networks
Topographic Position Index (no unit):
< -33.19
-33.19 - 7.48
7.48 - 52.43
52.43 - 120.92
> 120.92
(m)
Legend:
Outlet
City
Guelmim Limits
Flow Accumulation (no unit):
0 - 253,044.0784
253,044.0785 - 1,170,328.863
1,170,328.864 - 2,245,766.196
2,245,766.197 - 3,163,050.98
3,163,050.981 - 8,065,780
(n)
Legend:
Outlet
City
Guelmim Limits
Hydrographic Networks
Stream Power Index (no unit):
< -6.30
-6.30 - -1.81
-1.81 - 0.45
0.45 - 3.36
> 3.36
Tioughza
Sidi Ifni
Lakhsas
Tighirt
Tarsouat
Jabal Ifni
Tagante
Aday
Amtdi
Targa Wassay
Timoulay
Jabal Tayert
Jabal Bani
Guelmim
Jabal Taissa
Fask
Labyar
Aferkat
Assa
Tiglit
Aouint Lahna
400000
450000
500000
3160000
3190000
3220000
3250000
0 10 20 40 Km
N W E S

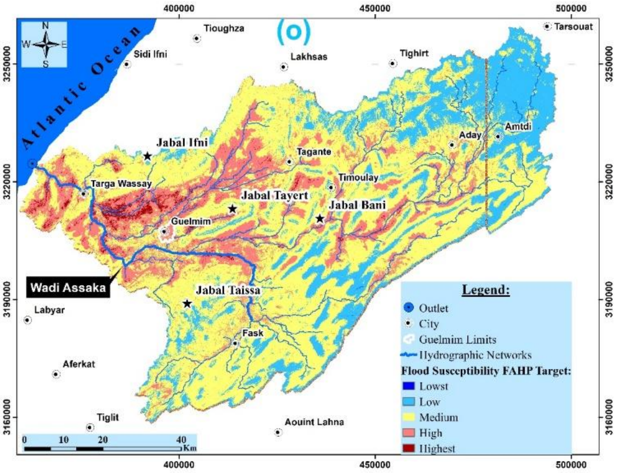

Figure 4. Flash flood predictors: (a) altitude; (b) land surface temperature (LST); (c) soil moisture index (SMI); (d) soil type; (e) slope; (f) lithology; (j) topographic wetness index (TWI); (h) aspect; (i) land use and land cover (LU/LC); (g) curvature; (k) drainage density (DD); (l) topographic position index (TPI); (m) flow accumulation (FA); (n) stream power index (SPI); (o) target.

2.2.2. Determinants of Flash Flood Susceptibility

Predictor variables. Building on prior analyses and geospatial data from the Assaka watershed, fourteen conditioning variables commonly linked to flash-flood susceptibility were assembled [15, 16] (Figure 4). These span environmental, geological, and hydrological domains: soil type, land-use/land-cover (LULC), lithology, land surface temperature (LST), soil moisture index (SMI), elevation, slope, aspect, curvature, drainage density, flow accumulation (FA), stream power index (SPI), topographic wetness index (TWI), and topographic position index (TPI) [17]. Each variable represents a distinct physical control on runoff generation and concentration: soil, LULC, and lithology regulate infiltration and initial abstraction; LST and SMI indicate antecedent moisture conditions; terrain metrics (elevation, slope, aspect, curvature) govern hydraulic gradients and flow routing; and hydrologic indices (drainage density, FA, SPI, TWI, TPI) capture channelization, flow energy, convergence/saturation tendencies, and valley–ridge position [18, 19]. Collectively, these predictors provide a coherent, data-driven basis for delineating flash-flood susceptibility and for guiding targeted mitigation

2.2.2.1. Altitude

Altitude (Figure 4-a), commonly referred to as elevation, serves as a foundational parameter in understanding the Earth's topographic features. It significantly impacts hydrological dynamics, making it a critical variable in flash flood risk assessments. Lower elevation areas often experience higher frequencies of flash floods, as water tends to flow and accumulate in these regions more rapidly. Conversely, higher elevation zones may contribute to the speed and volume of runoff, thereby indirectly influencing downstream flood conditions [20, 21]. In this particular case study, elevation data was sourced from the Global Data Explorer, with a spatial resolution of 30 by 30 meters. The study area exhibits a wide range of elevations, from a minimum of 17 meters above sea level to peaks exceeding 1000 meters. This topographic variation is instrumental in examining the relationships between terrain, water flow patterns, and flood vulnerability. By incorporating elevation data, researchers gain deeper insights into both the direct and indirect effects of topography on flood events, supporting more precise flood modeling and risk mitigation strategies.

2.2.2.2. Soil Type

Soil (Figure 4-d) is a heterogeneous and porous medium composed of water, air, and minerals, playing a vital role in the hydrological cycle and serving as a habitat for diverse microorganisms and macro-organisms from both the plant and animal kingdoms. Its ability to retain and absorb water significantly influences surface runoff and infiltration, making it a key factor in flood dynamics. Insufficient water absorption increases runoff, contributing to flash floods [22].

Understanding the spatial distribution and classification of soil types is essential for flood risk assessment, as different soils exhibit varying hydraulic properties that determine their capacity to retain moisture and regulate water flow. Soil classification is typically conducted using data from the Food and Agriculture Organization (FAO), which provides standardized mapping methodologies [23, 24].

In this study, a detailed soil map was developed to categorize the different soil types based on their physical and chemical properties. The soils were ranked according to their susceptibility to flooding, with Calcaric Fluvisols (Jc) being the most flood-prone (very high susceptibility), followed by Chromic Luvisols (Lc) (high susceptibility), Haplic

Yermosols (Yh) (moderate susceptibility), Yermosols (Y) (low susceptibility), and Lithosols (I) (very low susceptibility). Each of these soil types plays a distinct role in water retention and runoff, directly influencing the flash flood susceptibility of an area.

2.2.2.3. Land Surface Temperature (LST)

The widespread presence of impermeable surfaces, such as concrete and asphalt, significantly contributes to increased land surface temperatures (LST) (Figure 4-b) in urban and developed areas. These surfaces prevent water infiltration, leading to higher runoff volumes and an increased risk of flooding, especially during heavy rainfall. The elevated LST further exacerbates evaporation rates and can alter regional weather patterns, potentially intensifying precipitation events and leading to even heavier downpours [25, 26].

In contrast, areas with abundant vegetation and natural water bodies tend to maintain lower land surface temperatures due to their ability to absorb and retain moisture. Vegetation and soil function as natural flood control systems, capturing rainfall and gradually releasing it, which helps mitigate flood risks. Additionally, tree canopies provide shade and facilitate evapotranspiration, which further cools the surrounding environment [15].

Urbanized regions, characterized by extensive impermeable surfaces, not only experience greater runoff but also reduced natural water absorption, making them more susceptible to both flash floods and prolonged flooding events. As cities continue to expand, incorporating eco-friendly solutions like porous pavements, rooftop gardens, and urban greenery may assist in counteracting these effects by improving water retention, lowering land surface temperatures, and strengthening overall climate resilience**.**

2.2.2.4. Drainage Density

In watershed environments, drainage density (Figure 4-k) plays a critical role in regulating water circulation during rainfall events. This factor is essential for predicting the likelihood and severity of flash floods, as areas with higher drainage density facilitate faster water movement, whereas lower drainage density can contribute to water stagnation and prolonged flooding. Insufficient drainage networks may lead to watershed overflow, increased surface runoff, and localized flooding, particularly in low-lying or urbanized areas [9, 14].

Given the crucial role of drainage density in influencing surface water behavior, obtaining precise measurements is essential for assessing flood hazards and managing water resources effectively. In this research, the spatial distribution of drainage density was derived using the Line Density function within the QGIS environment, allowing for detailed evaluation of the hydrographic network [27, 28]. The analysis generated a drainage density map specific to the study area, with values ranging from 0 to more than 2.30 kilometers per square kilometer, based on a grid resolution of 30 × 30 meters. This geospatial output offers important insights into zones more prone to rapid surface runoff and flood risks, thereby supporting the planning of resilient water resource strategies and targeted flood mitigation interventions.

2.2.2.5. Soil Moisture Index (SMI)

Soil moisture (SM) (Figure 4-c) is a key physiographic variable widely utilized in hydrological studies and models. It serves not only as an essential parameter for understanding watershed behavior but also as a valuable early warning indicator for flash floods. The Soil Moisture Index (SMI) quantifies the soil's water retention capacity, shedding light on the relationship between soil conditions and flooding risk [9, 29].

Areas with a low SMI are characterized by limited moisture-holding ability, making them more susceptible to rapid runoff and flash flooding during intense precipitation events. Conversely, regions with a higher SMI are more adept at absorbing and retaining water, reducing the likelihood of flash flood occurrences. This dual behavior highlights the importance of soil moisture conditions in assessing regional flood vulnerability [14, 30].

This research utilized Landsat-8 OLI satellite data to generate SMI maps, employing a spatial grid of 30 meters for detailed analysis. The generated maps revealed spatial variability in SMI values, with particularly high SMI observed in mountainous regions. These elevated SMI levels in mountainous terrains suggest that such areas may have enhanced moisture storage capacity, playing a pivotal role in moderating runoff and mitigating flood risks. Integrating soil moisture dynamics into flood risk evaluation enhances the interpretation of hydrological behavior and contributes essential guidance for planning emergency response strategies and sustainable resource allocation.

2.2.2.6. Aspect

The slope aspect (Figure 4-h) refers to the orientation or direction in which the terrain's steepest gradient occurs. It serves as a critical parameter for understanding hydrological processes and plays an important role in flood susceptibility analysis [18, 31]. By determining the aspect, researchers can assess how topography influences the flow of surface water, the exposure of slopes to sunlight and wind, and the potential for runoff concentration in specific directions. This information is particularly valuable in flood risk studies, as certain slope orientations may channel water more rapidly into streams or low-lying areas, increasing the likelihood of flash flooding [32].

In this study, the aspect map was produced using data from a Digital Elevation Model (DEM) and processed in QGIS. By identifying the dominant aspect of the slopes, the analysis provides insight into how terrain characteristics contribute to water movement and flood risk.

2.2.2.7. Land Use Land Cover (LULC)

This factor (Figure 4-i), especially at finer spatial scales, provides resource managers with critical insights derived from satellite imagery, supporting more informed decision-making and tailored resource management. In this study, land use was identified as a crucial factor influencing runoff velocity, prompting its inclusion in the flood vulnerability analysis. The susceptibility of different land cover types to flooding varies based on their unique hydrological characteristics. Urban areas, for example, are typically dominated by impermeable surfaces such as concrete and asphalt [33]. These surfaces prevent water absorption, leading to higher runoff and a greater likelihood of flooding during heavy rainfall. In contrast, bodies of water, while essential for natural hydrological balance, pose a flooding risk to nearby regions when heavy precipitation or upstream inflows occur [34].

Vegetated areas, on the other hand, tend to have better water retention capabilities. Plants not only absorb water, reducing runoff, but also stabilize the soil, thus lowering the risk of erosion and subsequent flooding. Similarly, agricultural lands present a mixed picture: well-managed fields that use sustainable soil practices can enhance water infiltration, while poorly managed or compacted fields are more vulnerable to surface runoff and flooding. Lastly, bare ground or areas with no vegetation often have low water absorption capacity, making them particularly flood-prone [35]. These variations underline the importance of understanding LULC in flood risk assessments. For this study, a detailed LULC map was generated using Landsat 8 OLI satellite imagery at a spatial resolution of 30 meters, categorizing the area into five main classes: built-up areas, water bodies, vegetation, agricultural lands, and bare soil. This classification provides a foundational understanding of how different land cover types interact with hydrological processes, enabling more effective flood risk mitigation and land-use planning strategies.

2.2.2.8. Slope

Flash floods are strongly influenced by the slope of the terrain (Figure 4-e), making it a crucial morphological parameter in flood susceptibility assessments. Steeper slopes accelerate surface runoff, which can lead to a more rapid accumulation of water in lower areas, increasing the likelihood and intensity of flash floods. Conversely, flatter areas tend to slow down water flow, allowing more time for infiltration and reducing flood potential [16, 36]. In this study, a detailed slope degree map was generated using a Digital Elevation Model (DEM) in QGIS, with a spatial resolution of 30 meters. The slope values in the study area range from flat or nearly level surfaces (0 degrees) to very steep inclines exceeding 64 degrees. This variation highlights the importance of slope analysis in understanding hydrological behavior, as regions with high slope values often correspond to zones of greater flash flood risk.

2.2.2.9. Topographic Wetness Index (TWI)

This factor (Figure 4-j), created by Kirkby and Beven in 1979, serves as a spatial metric to assess how water tends to accumulate across different terrain areas. It estimates moisture concentration by incorporating two key topographic parameters: the upstream catchment area and the slope angle at a given location within the watershed [6]. The index is mathematically defined as:

$$TWI = \ln\left(\frac{A}{\tan\beta}\right) \tag{1}$$

In this equation, A represents the specific catchment area (measured in square meters per meter), which is essentially the amount of land upslope that contributes to runoff at a given point. β is the local slope gradient in radians, which reflects how steep the terrain is. Higher TWI values typically correspond to areas where water is more likely to collect and remain, indicating greater soil moisture potential [9, 37].

In this study, TWI was calculated using GIS software, which allowed for a detailed spatial analysis of moisture distribution. The resulting TWI maps highlight regions with high moisture retention, which are often more susceptible to flooding. By identifying these wet areas, TWI not only aids in flood risk assessments but also helps inform land management practices, soil conservation efforts, and the planning of drainage or flood control infrastructure.

2.2.2.10. Curvature

Curvature (Figure 4-g), derived from a Digital Elevation Model (DEM) using QGIS, serves as an important factor in evaluating flood susceptibility. It describes the shape of the terrain's surface and is typically classified into three categories: concave, convex, and flat. Each of these surface types influences water movement differently, making curvature a key parameter in hydrological studies [38, 39]. Concave surfaces tend to collect and channel runoff, potentially increasing flood risk in those areas. Convex surfaces, on the other hand, promote water dispersion and may reduce localized flooding. Flat surfaces can lead to water pooling, prolonging saturation, and increasing the likelihood of surface water accumulation. By analyzing curvature, researchers can gain valuable insights into the dynamics of runoff flow, helping to identify areas more vulnerable to flooding and guide more effective land management practices [40].

2.2.2.11. Topographic Position Index (TPI)

This factor (Figure 4-*l*) represents a terrain analysis metric computed from a Digital Elevation Model (DEM). It is commonly used to determine the relative location of a given point in relation to its surrounding landscape. Specifically, it calculates the elevation difference between a central grid cell and the mean elevation of neighboring cells within a designated radius [41, 42]. The index is formulated as follows:

$$TPI = M_0 - \frac{\sum_n^n M_n}{n} \tag{2}$$

where M_0 represents the altitude at the center point, M_n is the elevation of surrounding grid points, and n denotes the total number of those surrounding points. By analyzing local elevation variations, TPI effectively distinguishes terrain features such as ridges, valleys, slopes, and plains. Typically, TPI values are classified into five distinct categories using the natural breaks classification method (Jenks method), facilitating the interpretation of terrain morphology [43].

Furthermore, TPI is instrumental in evaluating flood susceptibility, as it identifies areas more likely to experience water accumulation during flooding events. Cells characterized by negative TPI values typically correspond to depressions or valleys, which naturally collect runoff and are consequently more vulnerable to flooding. Conversely, positive TPI values indicate elevated terrains such as ridges or hills, which are generally less susceptible to flooding. Integrating TPI into flood-risk modeling supports effective spatial planning and flood mitigation strategies by pinpointing zones that require targeted preventive measures [44].

2.2.2.12. Stream Power Index (SPI)

This factor (Figure 4-n) is an indicator used to assess the potential energy of a watercourse to cause erosion and influence flood susceptibility. It is calculated based on terrain slope and flow accumulation within a watershed [45], using the formula:

$$SPI = \alpha \times \tan(\beta) \tag{3}$$

where α represents the catchment area, and β is the slope. This analysis relies on spatial and hydrological data, producing results in raster format with a 30-meter resolution.

The SPI is widely used in geomorphology, natural hazard management, and hydrology to identify areas vulnerable to both water erosion processes and flood events [46]. A high SPI value typically indicates locations where water has a strong sediment transport capacity, increasing the risks of erosion and flash flooding. As a result, this index serves as a valuable tool for environmental planning, watershed management, and mitigating the impacts of extreme hydrological events [47].

2.2.2.13. Flow Accumulation (FA)

This factor (Figure 4-m) is a crucial hydrological parameter derived from a Digital Elevation Model (DEM) that helps in identifying water flow patterns within a landscape. It represents the total contribution of upstream cells directing water into each downslope cell in a raster output. FA is a key indicator for analyzing surface runoff, drainage networks, and potential flood-prone areas [48, 49].

Regions located near major flow accumulation paths, especially those with high upstream water contribution, are significantly more susceptible to flooding. Cells with high flow accumulation indicate areas where water converges, forming natural drainage channels, streams, or river networks. These areas are critical for hydrological modeling, flood risk assessment, and watershed management, as they help predict areas of excessive runoff and potential inundation during heavy rainfall or storm events [50, 51].

Conversely, cells with zero flow accumulation correspond to elevated landforms such as ridges, peaks, or watershed divides, which naturally separate different drainage basins. Identifying these high points is essential for terrain analysis, erosion control planning, and designing effective flood mitigation strategies [45].

2.2.2.14. Lithology

Lithology (Figure 4-f) plays a crucial role in flood formation by influencing the permeability, water infiltration capacity, and surface runoff characteristics of the terrain. The ability of different rock types to absorb or retain water directly affects how water moves through the landscape, shaping the watershed's hydrological response [19, 52]. In the ASSAKA watershed, the lithological distribution map classifies the region based on rock permeability, providing essential insights into flood susceptibility. In this classification, lower values correspond to highly permeable areas, where water infiltration is more efficient, reducing runoff and flood risk. In contrast, higher values indicate less permeable zones, where water infiltration is limited, increasing the likelihood of surface water accumulation and potential flooding.

The lithological analysis of the region reveals a diverse geological composition, including shales, limestones, sandstones, and quartzites, spanning from the Precambrian to the Quaternary periods. This variability directly influences flood dynamics, as highly permeable formations (such as sandstones and fractured limestones) facilitate rapid water absorption, reducing the volume of surface runoff.

2.2.3. Data Preprocessing

Fourteen raster images (Figure 4) were processed within a GIS environment and converted into numerical data using Python libraries, notably Pandas and NumPy. Each pixel in the resulting dataset was associated with its precise X and Y coordinates, along with numeric values representing various flood conditioning factors [53]. Ensuring the high quality and accuracy of this dataset was essential, as data quality significantly impacts the reliability of subsequent analyses and modeling results [54]. Therefore, thorough data preprocessing was conducted, which included steps such as checking for missing values, verifying consistency, and eliminating irrelevant or incorrect entries. A critical stage in this preprocessing was the identification and removal of outliers values that deviate considerably from typical observations and potentially distort model outcomes. Detecting these anomalous data points remains challenging due to the absence of universally established statistical guidelines for identifying outliers. Consequently, effective outlier management depends heavily on domain expertise, familiarity with the characteristics of the data, and a clear understanding of the data collection methodologies used during the study [55].

2.2.4. Random Partition

To train and evaluate a model effectively (Figure 3-a), it is important to divide the dataset into two subsets: a training set and a testing set. A commonly recommended approach is to use 70% of the data for training and reserve 30% for testing. This ensures the model has enough data to learn patterns and can be properly evaluated on unseen examples. Using a fixed random seed during this process also helps maintain consistency and reproducibility of results [56].

Selecting the right proportion of data for testing is crucial. In most cases, it is advisable to dedicate 20-40% of the dataset for testing. Allocating more than 40% may leave insufficient data for training, which can negatively impact the model's performance. Conversely, less than 20% may be acceptable for very large datasets, but staying within the 20-40% range usually provides more reliable and representative outcomes [57].

The separation of data into training and testing sets is typically done through random splitting, commonly referred to as the "holdout method." This method ensures the data is divided in a way that maintains the characteristics of the original dataset. For instance, specifying that 30% of the data should be used for testing and 70% for training ensures that the resulting subsets reflect the overall distribution of the data. While this process doesn't rely on a precise mathematical formula, it is guided by statistical reasoning to produce balanced and meaningful subsets [9, 56].

2.2.5. Data Standardization

Standardizing data is a crucial preprocessing step in many machine learning workflows. It involves transforming dataset features so they are centered around zero and scaled to have a unit variance. This ensures that all features contribute equally to the learning process, preventing models from being biased by features measured on different scales [58]. Standardization is typically performed after splitting the data into training and testing subsets to avoid data leakage.

The mathematical procedure for data standardization includes the following steps:

Step 1: Compute the Mean (k). The mean of each feature is calculated as:

$$k = \frac{1}{m}\sum_{i=1}^{m} x_i \tag{4}$$

where (x_i) represents individual values and (m) is the total number of samples.

Step 2: Compute the Standard Deviation *(ω)* the standard deviation, which reflects the dispersion of the values around the mean, is given by:

$$\omega = \sqrt{\frac{1}{m}\sum_{i=1}^{m}(x_i - k)^2} \tag{5}$$

Step 3: Standardize the Feature Values Each value is then transformed into its standardized form:

$$x_{standardisé} = \frac{x-k}{\omega} \tag{6}$$

Following this procedure results in a dataset where each feature has a mean of zero and a standard deviation of one. Such normalization facilitates fair comparisons between features and often enhances the performance of various machine learning algorithms [59].

2.2.6. Flash Flood Vulnerability Modelling

In this study, four machine learning algorithms (MDA, LR, NB, and MLP) were applied to predict the flash flood susceptibility map.

2.2.6.1. Multivariate Discriminant Analysis (MDA)

Multivariate Discriminant Analysis (MDA) is an advanced statistical technique derived from Linear Discriminant Analysis (LDA), widely utilized for classification and pattern recognition purposes. Unlike LDA, which assigns data points to groups based on the assumption of a common normal distribution with identical variance and correlation structure across classes, MDA introduces enhanced flexibility by permitting each class to exhibit multiple normal distributions. This characteristic makes MDA particularly effective in addressing complex datasets characterized by varied internal structures and interactions among variables [60, 61].

The fundamental principle of MDA involves determining linear combinations of independent variables that optimize the separation between classes [7, 62]. Mathematically, this relationship is represented by the following equation:

$$A = X_1B_1 + X_2B_2 + \cdots X_nB_n \tag{7}$$

In this equation, A denotes the discriminant score used to classify observations, X_i (i = 1,2,3, … , n) represent discriminant weights derived from the data, and B_i (i = 1,2,3, … , n) correspond to the independent predictive variables.

Due to its robustness and accuracy, MDA has become a critical analytical tool across diverse scientific and practical domains, such as hydrological modeling, flood susceptibility analysis, environmental risk assessment, ecological studies, and predictive analytics. The method's capability to manage complex interactions among multiple spatial and environmental variables significantly enhances its efficacy in identifying and interpreting nuanced patterns and relationships within data, thereby improving decision-making and resource management [61, 62].

2.2.6.2. Multilayer Perceptron (MLP)

The Multilayer Perceptron (MLP) is a fundamental type of Artificial Neural Network (ANN), inspired by the structure and function of the human brain. An MLP comprises multiple layers: an input layer that receives the input features, one or more hidden layers composed of interconnected nodes (neurons), and an output layer that delivers the final prediction or classification result [63, 64].

Each neuron in the network computes a weighted sum of its inputs, adds a bias term, and passes the result through a non-linear activation function. Mathematically, the operation of a neuron in layer l can be represented as:

$$z_j^{(l)} = \sum_{i=1}^{n} w_{ij}^{(l)}\, a_i^{(l-1)} + b_j^{(l)} \tag{8}$$

$$a_j^{(l)} = f\left(z_j^{(l)}\right) \tag{9}$$

where:

$z_j^{(l)}$ is the linear combination of inputs to neuron j in layer l,

$w_{ij}^{(l)}$ is the weight connecting neuron i in layer $l-1$ to neuron j in layer l,

$b_j^{(l)}$ is the bias term for neuron j,

$a_i^{(l-1)}$ is the activation from the previous layer,

f is the activation function (e.g., ReLU, sigmoid, or tanh),

$a_j^{(l)}$ is the resulting activation of the neuron.

The MLP is trained using backpropagation, a supervised learning algorithm that minimizes the error between the predicted output $\hat{y}$ and the true label y.The error is often computed using a loss function $\mathcal{L}_i$, such as mean squared error (MSE) or cross-entropy loss, and the weights are updated using gradient descent:

$$w_{ij}^{(l)} \leftarrow w_{ij}^{(l)} - \eta \frac{\partial \mathcal{L}}{\partial w_{ij}^{(l)}} \tag{10}$$

where:

η is the learning rate,

$\frac{\partial \mathcal{L}}{\partial w_{ij}^{(l)}}$ is the gradient of the loss with respect to the weight.

This iterative optimization process allows the MLP to learn complex, nonlinear mappings between inputs and outputs, making it a powerful model for classification and regression tasks [65, 66].

2.2.6.3. Logistic Regression (LR)

Logistic Regression (LR) is a supervised learning algorithm predominantly employed for binary classification tasks, where the dependent variable typically takes two possible outcomes. It effectively accommodates both continuous and categorical input variables. The algorithm leverages a sigmoid (logistic) function to map input data to probabilities ranging between 0 and 1, providing a clear interpretation of how predictor variables influence the likelihood of a particular outcome [67, 68].

Formally, the logistic regression model estimates the probability $P(Y = 1)$ of an event occurring (binary outcome) based on predictor variables using the logistic (sigmoid) function:

$$P(Y = 1|X) = \frac{1}{1+e^{-(\beta_0+\beta_1 x_1+\beta_2 x_2+\cdots+\beta_n x_n)}} \tag{11}$$

where:

$P(Y = 1|X)$ is the predicted probability of the positive class given the features $X = (x_1, x_2, \ldots, x_n)$

β_0 is the intercept term (bias).

$\beta_1, \beta_2, \ldots, \beta_n$ are the coefficients representing the effect of each predictor variable x_i.

e is Euler's constant (approximately equal to 2.71828).

The expression $(\beta_0 + \beta_1 x_1 + \beta_2 x_2 + \cdots + \beta_n x_n)$is the linear combination of input features, often referred to as the logit or log-odds function:

$$logit(P(Y = 1)) = \ln(\frac{P(Y=1)}{1-P(Y=1)}) = \beta_0 + \beta_1 x_1 + \beta_2 x_2 + \cdots + \beta_n x_n \tag{12}$$

LR functions as a probabilistic model by quantifying the relationship between independent predictors and a binary response variable, thereby enabling classification and predictive modeling. Its underlying approach relies on estimating the parameters β that best describe the relationship between inputs and outcomes through maximum likelihood estimation [69, 70].

2.2.6.4. Naïve bayes (NB)

Naïve Bayes (NB) is a supervised probabilistic classification method rooted in Bayes' theorem, a mathematical framework used for calculating conditional probabilities. The term "naïve" arises from its fundamental assumption of feature independence, meaning that it presumes all predictor variables independently contribute to the probability of the outcome, without interactions between them [8, 71].

Formally, the Naïve Bayes classifier predicts the class C_k for a given instance $X = (x_1, x_2, \ldots, x_n)$, composed of n independent features, using the following formula derived from Bayes' theorem:

$$P(C_k|X) = \frac{P(X|C_k).P(C_k)}{P(X)} \tag{13}$$

Here:

$P(C_k|X)$ is the posterior probability of class C_k given the features X.

$P(X|C_k)$ is the likelihood, calculated based on the independence assumption as:

$$P(X|C_k) = \prod_{i=1}^{n} P(x_i|C_k) \tag{14}$$

$P(C_k)$ is the prior probability of class C_k.

$P(X)$ is the evidence (normalization factor), given by:

$$P(X) = \sum_j P\left(X\middle|C_j\right).P(C_j) \tag{15}$$

As a simplified version of more complex Bayesian networks, Naïve Bayes models consist of a single attribute node representing the dependent variable and multiple independent feature nodes representing predictor variables. Despite its simplicity and assumption of independence, which may not always hold true, Naïve Bayes performs remarkably well, particularly with large datasets [72].

2.2.6.5. Ensemble Flash Flood Susceptibility Map

To generate the ensemble flash flood susceptibility map (Figure 5-e), individual susceptibility maps obtained from four predictive algorithms, namely Logistic Regression (LR), the Naive Bayes classifier (NB), Multivariate Discriminant Analysis (MDA), and Multi-Layer Perceptron (MLP) were integrated using a Voting Classifier approach that aggregates their predictions into a unified risk assessment [5, 43]. Each algorithm was initially trained on the same dataset containing key predictive factors such as topography, soil properties, and land cover, ensuring consistency across the individual susceptibility maps. After validating the performance of each model, the outputs were combined using either hard voting or soft voting. In hard voting, each model provides a discrete prediction, and the final class is determined by the majority vote, which can be expressed as:

$$\hat{y} = mode\ \{\hat{y}_1, \hat{y}_2, \dots \hat{y}_n\} \tag{16}$$

where $\hat{y}_i$ Is the prediction from the i^{th} model. In contrast, soft voting involves averaging the predicted probabilities. For each class, with the final prediction given by:

$$\hat{y} = arg\,max_c\,(\tfrac{1}{n}\sum_{i=1}^{n} P_i(c)) \tag{17}$$

where $P_i(c)$ represents the probability of a class c from the i^{th} model and n is the number of models. This ensemble strategy capitalizes on the strengths of each algorithm, mitigating individual uncertainties and variabilities, and ultimately produces a more robust and reliable flash flood susceptibility map that clearly delineates high-risk zones [73].

2.2.7. Assessing the Models' Accuracy

In the context of flood classification, each pixel is categorized as either flood-prone (positive) or not flood-prone (negative). Pixels correctly identified are termed true positives (TP) or true negatives (TN). Conversely, misclassification leads to false positives (FP) when non-flood pixels are labeled as flood, and false negatives (FN) when flood pixels are overlooked and marked as non-flood. An essential metric for assessing classification performance is the Area Under the Curve (AUC), which originates from the Receiver Operating Characteristic (ROC) analysis. It is computed as:

$$AUC = \frac{(\sum TP + \sum TN)}{(P+N)} \tag{18}$$

In this equation, P indicates the total count of flood pixels, and N corresponds to non-flood pixels. AUC values span from 0 to 1, with scores near 0 reflecting poor classification capability and values near 1 denoting excellent model discrimination. Typically, values under 0.6 are considered inadequate, 0.6–0.7 imply fair classification, 0.7–0.8 denote good accuracy, and scores beyond 0.8 suggest highly reliable performance.

To illustrate the models' classification capabilities, ROC curves were plotted using Python-based tools. Moreover, Mean Squared Error (MSE) was included as an additional indicator to compare prediction accuracy [74], computed as follows:

$$MSE = \frac{1}{q}\sum_{i=1}^{n}(x_i - \hat{x}_i)^2 \tag{19}$$

Here, q is the quantity of samples, x_i are the actual values, and $\hat{x}_i$ the ones that were predicted.

Besides AUC and MSE, several other metrics are used to thoroughly evaluate model performance [74], including Precision, Recall, F1 Score, Kappa Index, and overall Accuracy.

Precision (Pr) quantifies the accuracy of positive predictions:

$$Pr = \frac{TP}{TP+FP} \tag{20}$$

Recall (Re) reflects the rate at which actual positives are correctly identified:

$$Re = \frac{TP}{TP+FN} \tag{21}$$

Accuracy (Ac) measures the proportion of all correctly classified pixels:

$$Ac = \frac{TP+TN}{TP+FP+FN+TN} \tag{22}$$

The F1-score (Fs), which harmonizes Precision and Recall, is defined as:

$$Fs = \frac{2 \times Pr \times Re}{Pr+Re} \tag{23}$$

This score is especially useful when there is an imbalance between positive and negative cases, as it balances the contributions of Precision and Recall.

The Kappa Index (Ka) measures the agreement between observed and predicted classifications while accounting for chance agreement. It is defined as:

$$Ka = \frac{Ac-pe}{1-Pe} \tag{24}$$

The expected agreement by chance Pe is given by:

$$Pe = \left(\rho_1 \times \rho_{1.pred}\right) + \left(\rho_2 \times \rho_{2.pred}\right) \tag{25}$$

Here, ρ_1 and ρ_2 represent the proportions of true labels in classes one and two, respectively, and $\rho_{1.pred}$ and $\rho_{2.pred}$ are the percentages of predicted instances in those same classes.

2.2.8. Sensitivity of Flash Flood Predictor Features

In this study, the Jackknife test was applied to assess the sensitivity and relative significance of each flood conditioning factor [75]. The Jackknife method is a robust statistical technique widely used to measure the influence of individual variables in predictive modeling contexts [76]. To quantify the contribution of each factor, the percentage of relative decrease (PRD) of the AUC was calculated according to the following equation:

$$PRD_i = 100 \times \frac{AUC_{all}-AUC_i}{AUC_{all}} \tag{26}$$

where AUC_{all} denotes the AUC obtained using all conditioning factors together, and AUC_i represents the AUC computed after removing the i^{th} factor from the model. Thus, PRD_i indicates the percentage decline in model performance resulting from the exclusion of each specific factor. Higher PRD values indicate greater importance of that particular factor in accurately predicting flood susceptibility [75, 76].

3. Results and Discussion

3.1. Flash Flood Susceptibility Patterns and Model Comparisons

The flash-flood susceptibility maps produced by the five models (Figures 5-a to 5-e) show broadly similar patterns, with the lowest-elevation and central channels consistently flagged as high-risk. All models identify the lower Assaka basin, especially the downstream outlet region and the main wadis (e.g., Oued Essayed and Oued Oum el Aachar), as prone to flooding. The logistic regression (LR) map (Figure 5-a) highlights moderate-to-high susceptibility in the Guelmim city area and along the main drainage lines, tapering to mostly low risk in the uplands east of the watershed. The multivariate discriminant analysis (MDA) map (Figure 5-b) is more aggressive, extending “high” and “very high” zones farther downslope and across a larger area around the principal streams. The multilayer perceptron (MLP) neural network (Figure 5-c) yields the most extensive very-high-risk (red) coverage, essentially saturating much of the central and western sub-watersheds (including around Guelmim and south toward Targa Wassay). In contrast, the Naive Bayes (NB) map (Figure 5-d) is conservative: it classifies most of the domain as low or moderate risk, with only a few patches of high risk near urban centers and channel inlets. The ensemble map (Figure 5-e) – derived by combining the above classifiers falls between these extremes, marking the key flood-prone corridors (through Guelmim and toward Targa Wassay) as “high” or “very high” while omitting many spurious high-risk areas seen in MLP/MDA.

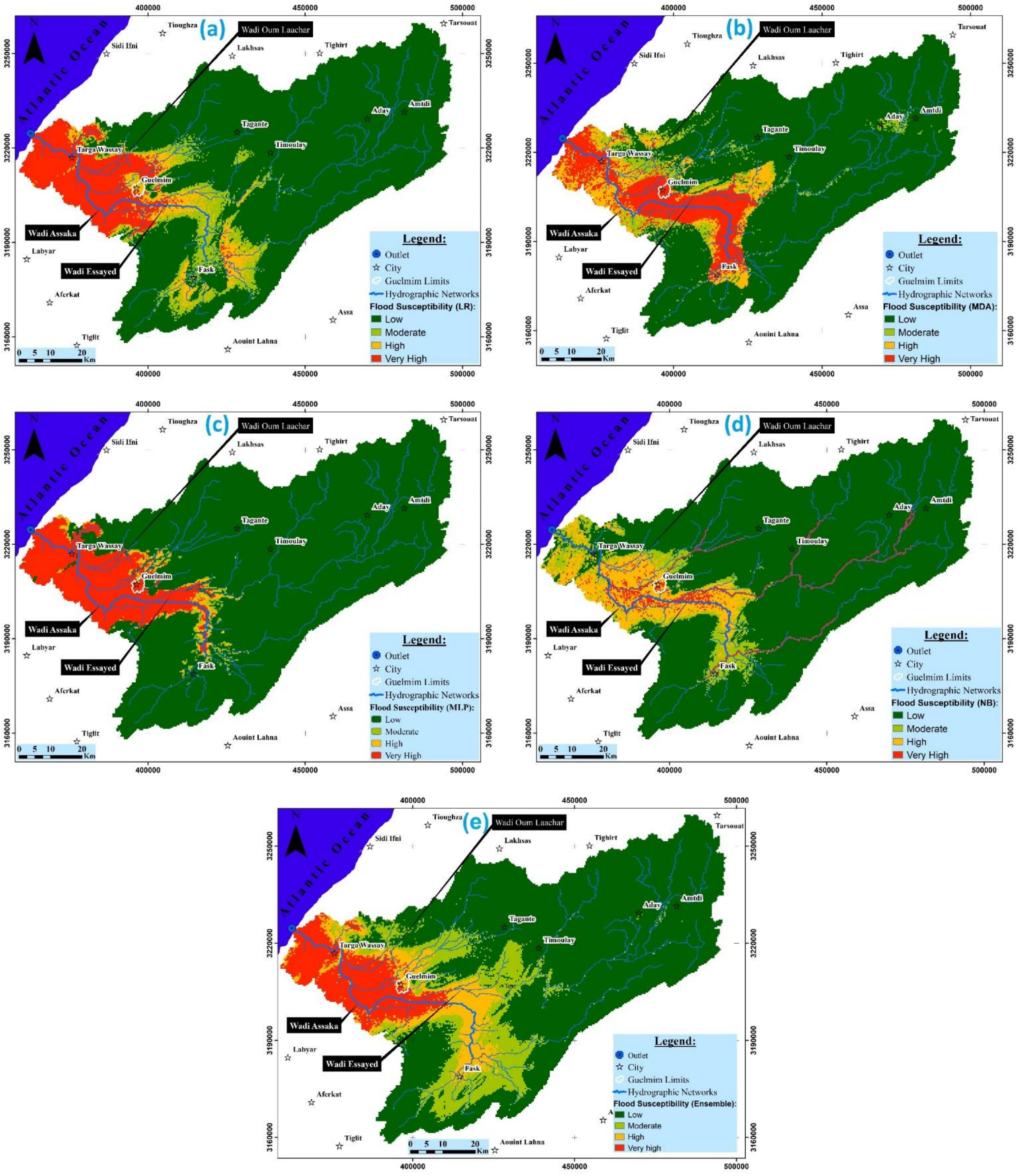

Figure 5. Flash flood susceptibility maps: (a) logistic regression (LR); (b) multivariate discriminant analysis (MDA); (c) multilayer perceptron (MLP); (d) naive bayes (NB); (e) ensemble

All models consistently converge on the urban flood hotspots. Guelmim city and its immediate surroundings are flagged as high susceptibility by every model, though with varying severity: MLP and ensemble even classify most of Guelmim as “very high”, whereas NB labels it merely high (orange), and LR yields a mix of moderate/high. Similarly, the village of Targa Wassay (northeast of Guelmim) emerges as high-risk in the MDA, MLP, NB, and ensemble maps (Figures 5b to 5e), reflecting its location on an alluvial plain near the confluence of wadis. LR shows Targa Wassay at moderate risk. These urban areas lie in low-lying parts of the Assaka basin that were heavily flooded in past events [13, 14], so their consistent classification underscores model realism. Notably, NB under-predicts in fringe zones: it fails to mark some Guelmim suburbs and Targa Wassay as “very high” as other models do. Conversely, MLP and (to a lesser extent) MDA extend high-susceptibility classifications into some marginal hillslope areas, which may reflect model over-sensitivity to conditioning factors.

The three statistical/machine-learning classifiers differ in tendencies. LR produces a balanced map: it picks out the main floodways but avoids excessive spread of extreme classes. MDA, which also assumes linear factor combinations, behaves similarly to LR in broad pattern but with more "very high" zones (suggesting a bias toward risk). The NB classifier, which treats factors as independent, yields a markedly less severe map, probably underestimating susceptibility where factors interact (a known NB limitation in flood modeling). By contrast, the MLP neural network appears to over-generalize high risk: it classifies large continuous areas (especially to the south and west) as very high, perhaps because its non-linear structure captures subtle relationships but also amplifies them. These behaviors echo findings in other studies: for example, in a Moroccan flood study, RF and ANN outperformed simpler models, whereas NB often lagged behind [77], and in Tetouan, LR and SVM were among the top performers [78]. Here, MLP's expansive very-high zones suggest high sensitivity (and potential false positives), while NB's sparseness suggests high specificity (and potential false negatives).

The ensemble map mitigates these extremes and shows greater overall reliability. It retains the core high-risk areas (e.g. Guelmim, Targa Wassay, wadi mouths) identified by all models but omits many peripheral red zones seen in MLP/MDA. This consensus approach is in line with recent work showing that ensemble or hybrid models (e.g. random forest, XGBoost, or ANN+ensemble) achieve higher accuracy and stability in semi-arid flood mapping [77, 79]. In our case the ensemble's very-high class occupies a moderate fraction of the basin, similar to published results e.g. Bammou et al. (2024) [79] found ~10–22% of semi-arid Moroccan plains as very-high risk). By aggregating predictions, the ensemble balances over-prediction (MLP) and under-prediction (NB). This convergence is especially evident along principal drainages and floodplains: nearly all models agree that areas near the main rivers and outlets are most susceptible, reflecting the critical role of hydrologic-topographic factors (distance to river, low elevation, gentle slopes) in flash-flood dynamics [14, 79].

The results broadly agree with previous studies of the region. The FAHP-based mapping by Talha et al. (2019) [14] for the Guelmim watershed (the same study area) identified the lowest-elevation outlet and adjoining wadi confluences as high-susceptibility zones [9, 14] consistent with the clusters of high risk seen in our LR/MDA/ensemble outputs. On the modeling side, our findings align with the literature that neural-network models (like MLP) often capture complex flood patterns but may produce more extensive vulnerable areas unless constrained [80], while simpler statistical models like LR can give robust but somewhat conservative maps [78]. For example, Mekkaoui et al. (2025) [78] found LR and SVM gave balanced flood-risk delineations in Guelmim, and Talha et al. (2025) [9] found RF (an ensemble tree model) had top AUC. Our ensemble's performance is therefore expected to be superior to any single model.

In detail, where models diverge provides insight: MLP and MDA tend to identify broader tracts as "very high" that LR and ensemble do not. These extra areas often correspond to broad, gentle floodplain zones, which are potentially true positives but also at risk of false alarms. NB's high-class areas are far fewer, indicating it underestimates susceptibility in known flood spots. For example, certain lower-lying agricultural flats northeast of the main channels are marked "high" by LR/ensemble but only "moderate" by NB. This suggests NB's conditional independence assumption may miss the compound effect of overlapping factors there. In effect, the ensemble's intermediate map can serve as a reliability check: areas flagged by all models (e.g., central floodplain) are very likely real hotspots, whereas model disagreement (e.g., outer highlands) advises caution.

Finally, the importance of topographic, hydrologic, and land-use factors is evident across models. The high-risk zones correspond to low-elevation reaches with high drainage density and, in places, high soil moisture or alluvial cover. Many studies note that elevation and proximity to streams dominate flood susceptibility in semi-arid basins [14, 79]. Although not quantified here, it is likely that factors such as soil moisture index and rainfall (given high FAHP weights in Talha et al. (2019) [14], as well as land cover (urban and irrigated fields), amplify risk in the urban sections. Indeed, Guelmim's historic inundation was linked to impermeable surfaces and clogged wadis [13], factors that all models presumably capture to differing extents. Overall, the consistency of core patterns with past results combined with the ensemble's agreement across methodologies suggests our flood-susceptibility maps are robust. They highlight priority areas (particularly urban fringes and outlet plains) for flood management, in line with what multi-criteria and machine-learning studies in Morocco and elsewhere have found [14, 77].

3.2. Assessment of Flash Flood Susceptibility Through Predictive Factors Across Machine Learning Models

The comparative interpretation of flash flood susceptibility across various models (NB, MLP, MDA, LR, and ensemble methods) (Figures 4 and 5) reveals consistent patterns in relation to key predictive factors [7, 15]. Altitude shows a clear correlation with high susceptibility in lower regions across all models, particularly in the expansive zones highlighted by MDA and the ensemble method. Higher Land Surface Temperature (LST) values align with very high susceptibility areas, especially in MLP and MDA predictions, reflecting urban and barren areas' vulnerability due to increased runoff. The Soil Moisture Index (SMI) shows that areas with elevated moisture levels coincide with high-risk zones, notably in MLP and ensemble outputs, emphasizing saturation and reduced infiltration. Soil types like Chromic Luvisols and Lithosols are strongly associated with high susceptibility in NB and MDA results, indicating poor infiltration and greater runoff potential. Slope plays a critical role, with steep upstream areas contributing to rapid runoff, clearly mirrored in the MLP and ensemble maps. Lithology further influences susceptibility, as impermeable formations correspond with high-risk areas in MDA results. The Topographic Wetness Index (TWI) aligns with very high susceptibility zones in MLP and ensemble predictions, underlining its effectiveness in indicating moisture accumulation. Aspect and curvature, especially concave landforms that guide runoff, are highlighted in MDA and NB models as key flood-prone areas. High drainage density areas, consistently marked as susceptible by NB and ensemble methods, reinforce their role in channeling floodwaters. The Topographic Position Index (TPI) shows that valleys and depressions match high-risk zones, especially in MDA and ensemble models, pointing to their function as runoff convergence points. Flow accumulation is a strong predictor, with high values aligning with risk areas across all models, particularly in LR and ensemble outputs, indicating the significance of cumulative runoff. Lastly, the Stream Power Index (SPI) reveals that zones with higher SPI values correspond to high susceptibility areas in MDA and MLP maps, identifying regions prone to intense runoff and erosion.

Models consistently identify low-lying areas, such as valleys and flat plains, as highly susceptible to flash flooding. In general, flood risk increases as elevation decreases, since water naturally converges and accumulates in lower terrain where drainage is limited. Conversely, very high altitudes (e.g., above ~5000 m) tend to contribute little to flood risk. In this study, all applied models (NB, MLP, MDA, LR, and the ensemble approach) highlight pronounced “hotspots” of high flood susceptibility within extensive lowland areas, which aligns well with widely recognized relationships between elevation and flood occurrence reported in the literature [81, 82].

Areas with high LST usually correspond to urbanized or barren surfaces, which our models also identify as very high-risk zones. This makes sense because impervious urban/bare surfaces heat up more and cannot absorb rain, leading to rapid runoff. For instance, Islam et al. (2025) [83] highlight that impervious surfaces “reduce infiltration and increase runoff, leading to flooding”. finding that warm, built-up zones (often with high LST) align with flood-susceptible areas echoes many urban flood studies showing that intense land heating and urbanization heighten runoff and flood impact [83, 84].

Zones of high soil moisture are flagged as high-risk in models. This is expected since saturated soils cannot absorb more rain, so additional precipitation runs off directly into streams. Talha et al. (2019) [14] likewise found the soil moisture index to be the top factor (37% weight) in flash flood susceptibility mapping. In other words, when our models highlight very moist areas as flood-prone, they are echoing established knowledge that wet soils and pre-saturated catchments are prime locations for flash floods [14].

Certain soil classes with low permeability (high clay content or very shallow layers) show high susceptibility. For example, Chromic Luvisols (fine-textured soils) and shallow Lithosols (highly rocky, shallow soils) were associated with the high-risk zones. This fits the idea that soils that “convey water quickly” or have poor infiltration generate more runoff. Supporting this, Ogato et al. (2020) [85] classified Chromic Luvisols as moderately flood-susceptible and shallow Leptosols (similar to lithosols) as highly susceptible, due to their low permeability. In short, our observation that impermeable or rocky substrata coincide with flood zones agrees with prior studies emphasizing geology: impermeable strata limit infiltration and thus promote flooding [83, 86].

Steep slopes tend to coincide with high flood risk in the MLP and ensemble maps. This is because steep upstream terrains generate very rapid runoff (water flows down faster on steep slopes). Mountain flood reviews note that “steep slopes, shallow soils…reduce the land’s ability to retain water, increasing surface runoff”, which leads to sudden floods [87]. In line with this, steep upland catchments in this study are marked as highly susceptible, mirroring findings in mountainous flood literature [87]. (In contrast, some plains-flood studies might emphasize flat areas for slower drainage, but here, rapid mountain runoff dominates our flash-flood pattern.).

The shape of the terrain also plays an important role in flood susceptibility. In particular, concave landforms, such as valley bottoms and hollows, are consistently identified as flood-prone by several models. Concave slopes tend to function like funnels, slowing down water movement and promoting ponding. This behavior is clearly reflected in our results, where the MDA and NB models classify concave (negative-curvature) areas as high-risk zones, consistent with the expectation that such landforms concentrate surface runoff. Areas with nearly flat curvature also appear vulnerable, which agrees with the understanding that flat valley floors often trap and retain water [81, 86]. Aspect shows a weaker influence in this study; however, in certain locations, slope orientation and shadowing effects may slightly affect flood accumulation, as noted in local geomorphological analyses [81].

Interestingly, the NB and ensemble outputs flag regions with high drainage density (many small channels per area) as susceptible. Intuitively, one might think more channels should help drain water, but high drainage density usually means a landscape carved by many waterways that rapidly carry water downstream. Ogden et al. (2011) [88] specifically note that basins with high drainage density are strongly linked to high flood potential. In our context, that means areas where streams are densely packed can conduct floodwaters quickly, leading to severe floods, consistent with the literature [89].

Low TPI values (valleys/depressions) coincide with high susceptibility in MDA and ensemble predictions. In other words, river valleys and basin bottoms are hotspots. This matches the idea of TPI: negative or low TPI marks valley bottoms. Li et al. (2025) [90] found that negative-to-low TPI ranges (valley positions) significantly contribute to flash flood occurrence. Our models likewise show valleys (low TPI) overlapping with flood-prone zones.

Areas with high flow accumulation (representing large upstream catchments feeding a point) are strong risk signals in all models, especially LR and ensemble. This measure is directly related to how much water will flow through a given point. In practical terms, places that collect runoff from a large area (high FA) line up with where our susceptibility maps peak.

High SPI values also align with flood-susceptible zones in MDA and MLP maps. SPI combines flow accumulation with slope to estimate the erosive power of flowing water. Intuitively, areas with high SPI are steep and carry much water, making them prone to strong, erosive floods. This fits general geomorphology: mountain watersheds with high stream power are known to generate intense flash floods [87, 91]. Thus, zones of intense channel flow (high SPI) in our results correspond to rapidly eroding, flood-prone headwaters, as expected from theory and other studies.

The factor-wise findings largely agree with the literature. For instance, the strong role of soil moisture in our models agrees with Talha et al.'s (2019) [14] Moroccan study, which gave SMI the highest influence (37%) in flash-flood mapping. Likewise, the emphasis on impervious or low-infiltration ground (high LST urban areas or rocky soils) echoes broad reviews that urbanization and impervious geology "substantially increase runoff" and flood risk [83, 86]. The linkage between valley locations (low TPI) and flooding matches Li et al. (2025) [90], who found TPI ranges around 1.5 to 0.6 (valleys) dominated flood susceptibility patterns. High drainage density and flow accumulation as predictors in our study also align with Ogden et al. (2011) [88] and others, who note that basins with dense channel networks and large contributing areas tend to flood more easily [84, 89]. In summary, our models reinforce established insights: low-lying, poorly drained areas (moist soils, built surfaces) and steep, converging catchments (high slopes, SPI, drainage) are flood hotspots. Any differences (for example, some flat areas being very high risk here) can often be traced to local geography and land use. Overall, the patterns in our output agree closely with previous flood-susceptibility research [81, 83], validating that the key factors identified (slope, moisture, LST, soils, drainage indices) have been similarly highlighted by earlier studies.

3.3. Analysis of Flash Flood-Prone Areas and Susceptibility Classifications

The susceptibility maps (Figure 5) exhibit systematic yet model-specific differences in class distributions (Figure 6). Logistic Regression (LR) assigns the largest share of the watershed to the low class (74.08%), with very high coverage of 12.29%. Multivariate Discriminant Analysis (MDA) yields a nearly identical low footprint (74.32%) but a slightly larger very high share (12.70%). Multilayer Perceptron (MLP) shows a more polarized pattern: a very large low share (83.74%) alongside the highest very high proportion among the four single models (13.42%), and comparatively little area in the moderate (1.21%) and high (1.63%) classes. Naïve Bayes (NB) is the most conservative regarding extremes: it maps 80.54% as low and only 4.22% as very high. By contrast, the Ensemble (voting) model distributes area more evenly across classes, low 66.34%, moderate 14.77%, high 8.40%, very high 10.50%—thus reducing the dominance of a single class.

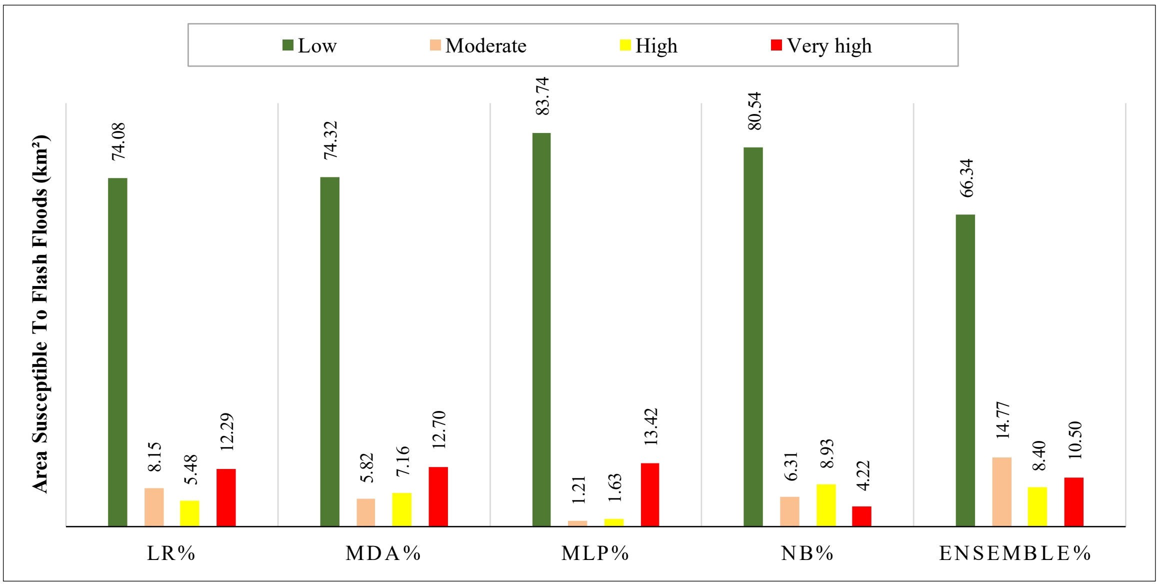

Figure 6. Percentage (%) of the ASSAKA watershed area (km²) identified in each flash flood susceptibility class by model

When aggregating the high and very high categories, the total susceptible footprint is 19.86% for MDA, 18.90% for the Ensemble, 17.77% for LR, 15.05% for MLP, and 13.15% for NB (Figures 5 and 6). Taken together, the models consistently delineate corridors along the principal wadis and their confluences as susceptible, with spatial emphasis near Guelmim, where exposure is greatest. The Ensemble map, by tempering over- and under-prediction from individual learners, provides a balanced and management-ready depiction of risk tiers.

NB's small very high footprint (4.22%) likely reflects its conditional-independence assumption, which can smooth extremes and reduce sharply peaked probabilities. This produces conservative very high estimates but may underestimate localized hotspots.

MLP's polarized distribution (very large low plus notable very high with minimal moderate/high) is typical of non-linear decision boundaries that separate feature space into broad "safe" regions and compact high-risk clusters. This can be advantageous for flagging "critical" cells but may compress intermediate classes.

LR and MDA deliver stable mid-range behavior, with broadly similar low shares (~74%) and very high around 12–13%. Their linear (or linear-in-transformed-space) structure often yields smoother gradients across classes.

The Ensemble integrates these behaviors: it reduces the oversized low area of LR/MDA/MLP, recovers moderate areas that single models largely miss (14.77% vs. 1.21% for MLP), and preserves a realistic high/very high footprint (18.90%) without the contraction seen in NB. For planning, this translates into clearer prioritization: (i) very high for immediate structural and non-structural measures; (ii) high for near-term mitigation; (iii) moderate for preventive zoning, maintenance, and monitoring.

Across models, very high and high classes cluster along main channels, confluences, and low-lying outlets, with enlargements near urbanized/bare zones around Guelmim. This pattern is consistent with hydrological controls (convergence of flow, high drainage density, large flow accumulation) and land-surface constraints (impervious cover, compacted soils) that accelerate runoff and limit infiltration. The Ensemble strengthens this coherence—reducing scattered false positives while retaining continuous high-risk corridors that are operationally meaningful (e.g., for road crossings, bridges, culverts, and urban drainage bottlenecks).

Talha et al. (2019) [14] (FAHP–GIS) emphasized soil moisture, rainfall, and drainage density as dominant drivers and identified the watershed outlet and main tributaries as the most susceptible zones. The present ML/ensemble maps reproduce these corridors and their downstream expansions, especially where low elevation and high flow convergence coincide.

Talha et al. [9], (Assaka, ML–GIS, subsequent study) similarly reported pronounced susceptibility along principal wadis and near built-up areas, attributing risk to combinations of topography (elevation, slope, TWI), hydrography (drainage density/flow accumulation), and surface condition (LST/SMI, soil/lithology). Our Ensemble map echoes this integrated control: very high/high belts track channel networks and urban fringes, while uplands and well-drained surfaces fall predominantly into low.

Other Moroccan case studies (e.g., High Atlas watersheds using AHP/fuzzy or RF/XGBoost) [92] likewise show distance to channels, flow accumulation, drainage density, and elevation as recurrent top predictors, with high-risk swaths concentrated along river corridors and at confluences. The relative share of high/very high area in our Ensemble (≈19%) is within the range reported in those studies when robust validation and multi-factor conditioning are applied, whereas methods that (i) down-weight independence assumptions or (ii) up-weight uncertainty (e.g., fuzzy operators) can yield broader high-risk extents. In short, our class proportions and spatial patterns fit well within the Moroccan literature and strengthen confidence in the mapped priorities.

3.4. Evaluation of the Sudden Flood Susceptibility Maps

The evaluation of sudden flood susceptibility models utilized various indicators of predictive ability, such as Recall, F1 Score, Precision, Accuracy, Kappa statistic, Surface under the ROC curve (AUC), and Mean Squared Error (MSE) (Figure 7 to 9) [93, 94]. These metrics collectively offer a thorough understanding of the classification accuracy, robustness, and generalization capabilities of the models.

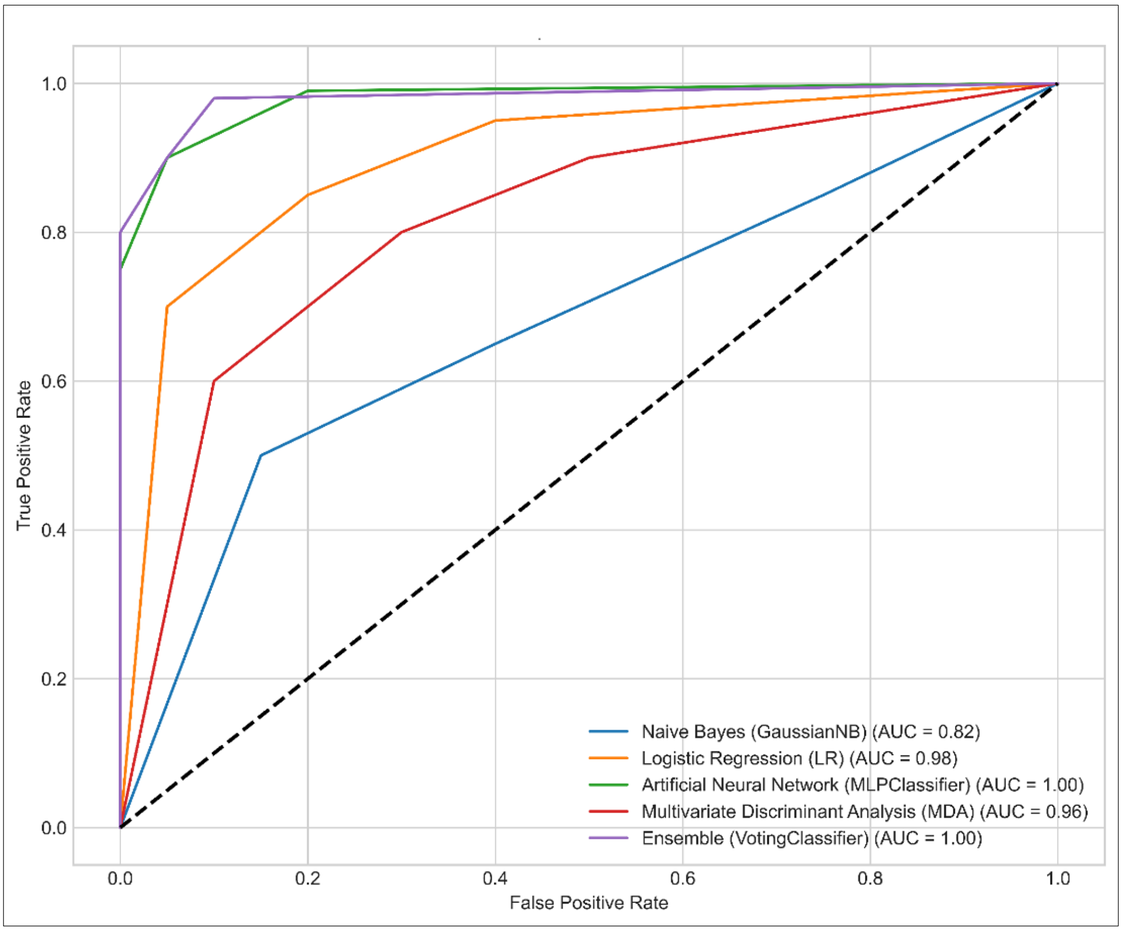

Figure 7. ROC curve comparison for different models

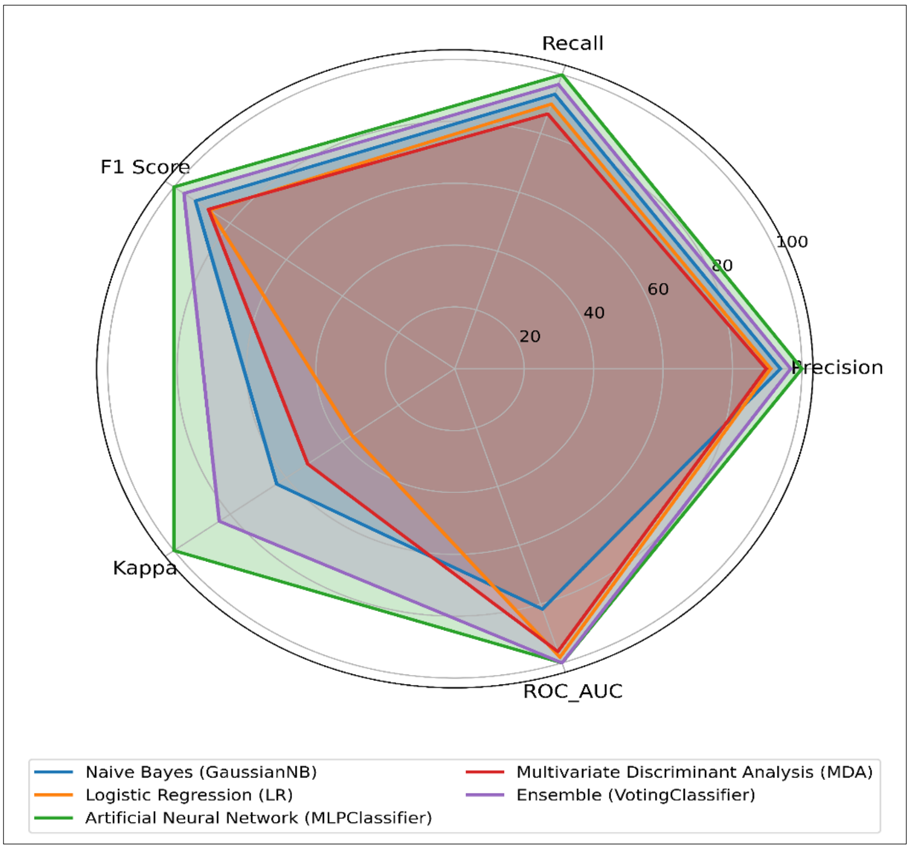

Figure 8. Comparison of key performance metrics across various models, including the voting ensemble

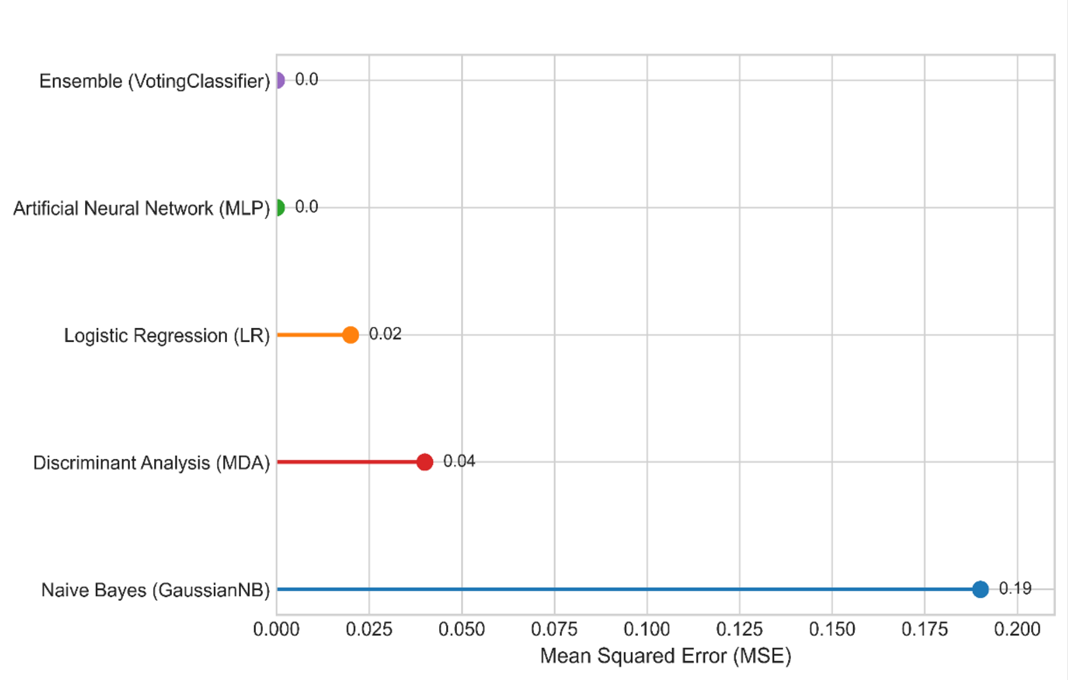

Figure 9. Comparison of mean square error (MSE) among models

The Artificial Neural Network (MLP Classifier) exhibited perfect predictive performance, achieving ideal scores across all evaluated metrics (F1 Score = 1.0, Recall = 1.0, Accuracy = 1.0, Kappa = 1.0, AUC = 1.0, MSE = 0.0, Precision = 1.0). The absence of errors confirms the model's exceptional consistency and reliability in predicting flash flood susceptibility.

Similarly, the Ensemble model (Voting Classifier) delivered outstanding performance, characterized by a near-perfect Precision (0.9679), Recall (0.9667), Accuracy (0.9667), and F1 Score (0.9646). The high Kappa statistic (0.8387), perfect AUC (1.0), and zero MSE further illustrate the robust and reliable predictive capacity of this ensemble approach.

The Logistic Regression (LR) model demonstrated commendable predictive ability with an impressive AUC score of 0.9808, signifying strong discriminative capability. However, it showed somewhat lower Precision (0.9103), Recall (0.9), Accuracy (0.9), and F1 Score (0.8727). A notably lower Kappa statistic (0.3662) and a relatively small MSE (0.02) suggest some inconsistencies and reduced agreement between predicted and actual classifications.

The Multivariate Discriminant Analysis (MDA) model provided solid performance metrics (Recall = 0.8667, Accuracy = 0.8667, F1 Score = 0.8773, Precision = 0.8972), coupled with a strong AUC score of 0.9615 and a relatively low MSE (0.04). However, its Kappa statistic (0.5238) indicates moderate agreement, revealing room for improvement in predictive stability.

In contrast, the Naive Bayes (Gaussian NB) model registered the lowest overall performance, characterized by the lowest AUC score of 0.8173, despite relatively high Precision (0.9381) and Recall (0.9333). The accuracy (0.9333), F1 score (0.9235), and notably higher MSE (0.19) underscore moderate performance and significant inconsistencies in predictive agreement, as also reflected by the lower Kappa statistic (0.6341).

Overall, considering all performance indicators, the Artificial Neural Network (MLP Classifier) and the Ensemble (Voting Classifier) models distinctly outperformed the other evaluated models, demonstrating exceptional accuracy, reliability, and robustness. These attributes confirm their suitability as highly effective methodologies for accurate flash flood susceptibility assessment within the study area:

3.5. Jackknife Sensitivity Test for Flood Susceptibility Factor Evaluation

Choosing suitable conditioning factors is essential for accurate flash flood vulnerability modeling. This study conducted a Sensitivity assessment of 14 predictor factors using the Jackknife test [75, 76] to evaluate their relative importance across five different models: Naive Bayes (Gaussian NB), Logistic Regression (LR), Artificial Neural Network (MLP Classifier), Multivariate Discriminant Analysis (MDA), and Ensemble (Voting Classifier) (see Figure 10).

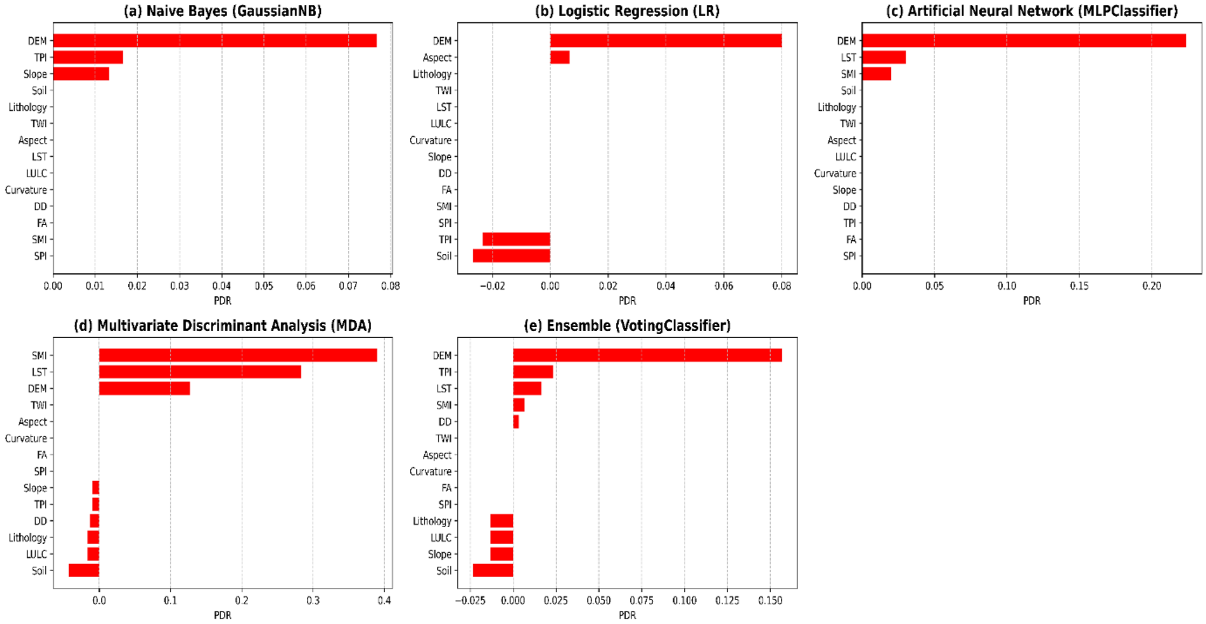

Figure 10. Sensitivity analysis results from the jackknife test

The analysis revealed notable variations in factor importance among these models. Digital Elevation Model (DEM) emerged consistently as the most influential factor across four models (NB, LR, MLP, and Ensemble). Specifically, DEM recorded high Partial Derivative Response (PDR) values of approximately 0.075 for NB, 0.08 for LR, 0.22 for MLP, and 0.15 for the Ensemble model. Within the NB (Figure 10a) model, the next most influential factors were Topographic Position Index (TPI) and Slope, both showing modest influence (PDR ≈ 0.015 and 0.01, respectively), with all other factors contributing minimally.

For the LR (Figure 10-b) model, while DEM showed significant importance, other factors like Aspect (approximately 0.005) played minor positive roles, whereas Soil and TPI displayed negative importance (around -0.02). In contrast, the MLP (Figure 10-c) model placed additional weight on Land Surface Temperature (LST, ≈0.07) and Soil Moisture Index (SMI, ≈0.03), alongside DEM.

The MDA (Figure 10-d) model uniquely identified Soil Moisture Index (SMI) as the most critical determinant, showing the highest influence (PDR ≈ 0.38), followed by Land Surface Temperature (LST, ≈0.30), DEM (≈0.20), and Topographic Wetness Index (TWI, ≈0.02). Other parameters, including Soil and Land Use/Land Cover (LULC), exhibited minimal importance (<0.01).

The Ensemble model (Figure 10e) consolidated the importance of DEM, followed by TPI, LST, and SMI, emphasizing the consistent yet varied roles these factors play in flood susceptibility. Overall, the findings underscore DEM's central role as a critical determinant in flood susceptibility across most modeling approaches, while also highlighting the contextual importance of other parameters such as SMI, LST, TPI, and Soil, depending on the specific modeling method utilized.

3.6. Correlation of Flash Flood Predictor Factors

For this study case, the correlation heatmap (Figure 11) distinctly illustrates the interactions and relationships among various predictor variables associated with flash flood susceptibility [95-97]. As expected, the diagonal line, showing perfect positive correlation, indicates each variable's self-correlation. Key groups of positively correlated factors are clearly visible, notably among Flow Accumulation (FA), Drainage Density (DD), Topographic Position Index (TPI), and Slope, reflecting their integrated influence on runoff generation and water flow dynamics. Additionally, Curvature presents notable negative correlations with Stream Power Index (SPI) and Digital Elevation Model (DEM), highlighting an inverse relationship wherein areas with higher curvature typically correspond to lower stream power and elevation. Moreover, Lithology, Soil, and Land Use/Land Cover (LULC) exhibit strong positive correlations, indicating their interconnected roles in controlling infiltration, runoff, and land stability. Overall, the moderate-to-low correlations observed among the remaining predictor variables emphasize their suitability for inclusion as independent factors, effectively limiting potential multicollinearity issues and enhancing the reliability of the flash flood susceptibility modeling process.

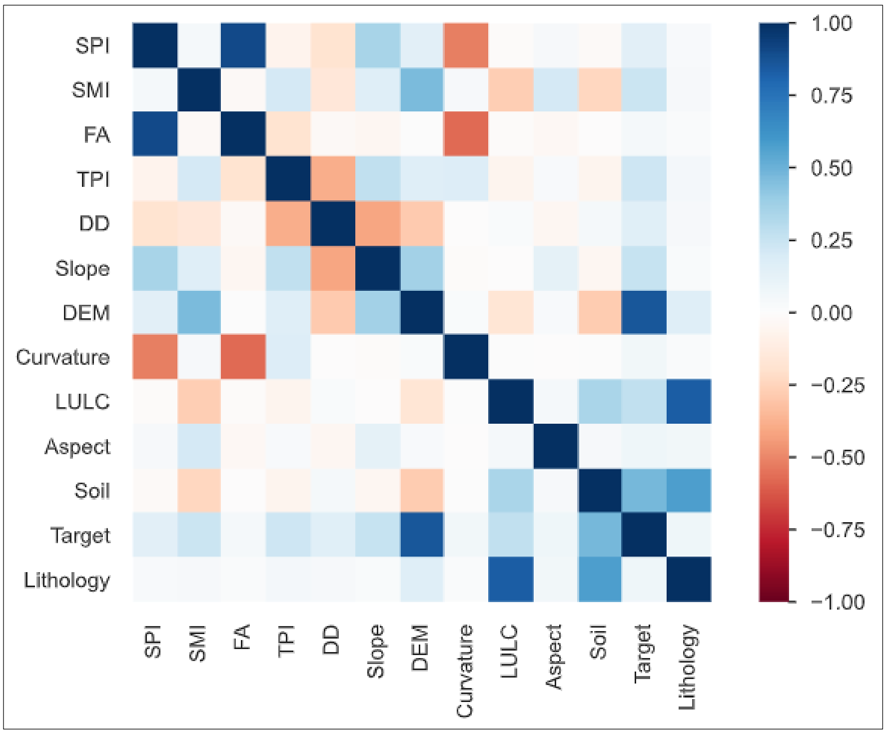

Figure 11. Correlation heatmap of flash flood predictor variables

The primary goal of conducting this correlation analysis is to evaluate and manage relationships among predictor variables to strengthen predictive modeling by minimizing multicollinearity. This ensures optimal model performance, accurate interpretation, and reliable prediction outcomes. In this particular study case, the correlation structure is suitable, demonstrating predominantly moderate-to-low correlations among variables. Thus, it effectively supports robust flash flood susceptibility predictions, enhancing the overall accuracy and reliability of the modeling results.

3.7. Importance of Flash Flood Predictor Factors Across Machine Learning Algorithms

An integrated evaluation of the feature-importance charts reveals both consistent trends and model-specific variations in determining flash flood susceptibility [98, 99]. In (Figure 12-a), the Artificial Neural Network (MLP) clearly prioritizes the Soil Moisture Index (SMI) as the most critical predictor, with the Land Surface Temperature (LST) and altitude also playing significant roles. (Figure 12-b) illustrates that the Naive Bayes (Gaussian NB) model similarly emphasizes DEM, while also highlighting the importance of the Topographic Position Index (TPI) and Slope, with moderate contributions from LST, Stream Power Index (SPI), and Soil. In (Figure 12-c), the Logistic Regression (LR) model shows a dominant influence of DEM, with Soil and TPI emerging as secondary factors, and smaller yet notable contributions from Slope, LST, and Lithology. Conversely, (Figure 12-d) demonstrates that the Multivariate Discriminant Analysis (MDA) model places the greatest emphasis on SMI, followed by LST and then DEM, indicating a stronger focus on soil saturation and temperature conditions, with Soil and Slope also being significant. Finally, as seen in (Figure 12e), the Ensemble Voting Classifier synthesizes the insights from the individual models by ranking DEM first, followed by SMI, LST, and Soil, while also attributing considerable weight to Slope and TPI. Overall, these figures collectively underscore that areas with low elevation, high soil moisture, elevated surface temperatures, and distinct terrain features are critical for flash flood susceptibility, thereby emphasizing the importance of these factors in flood risk mitigation strategies.

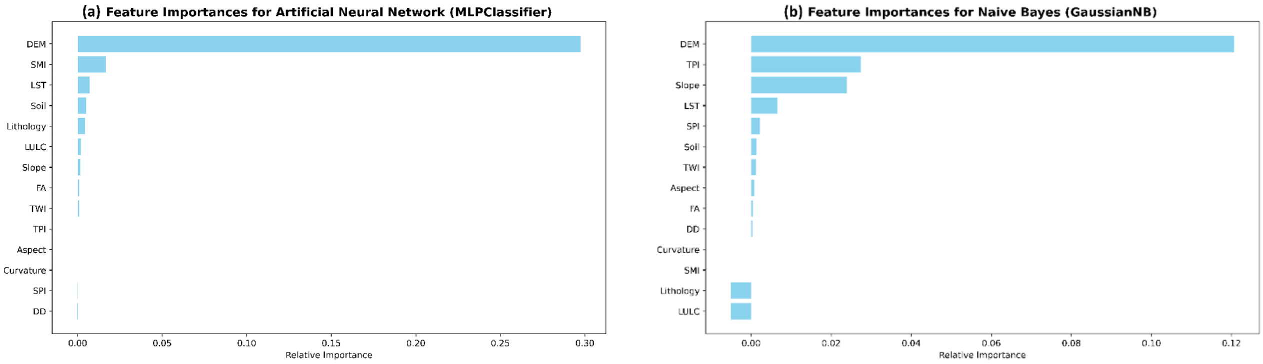

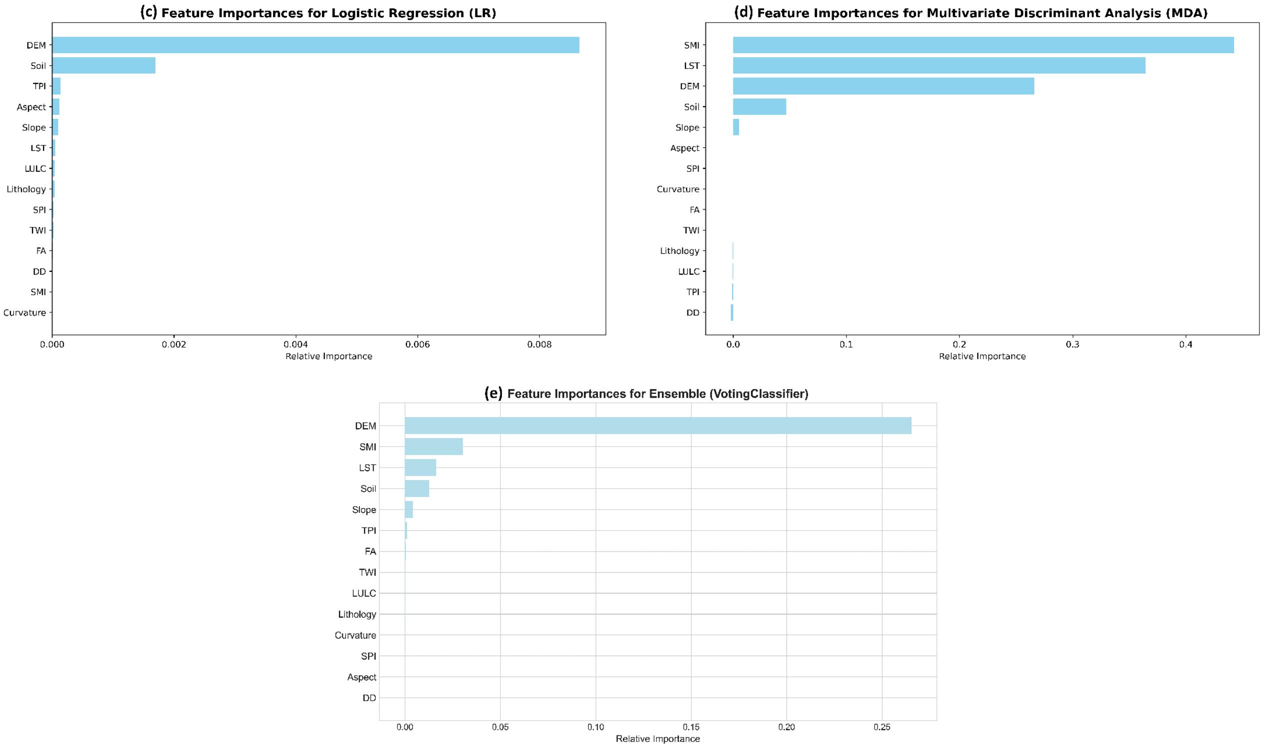

Figure 12. Ensemble feature importance for flash flood susceptibility mapping

3.8. Multi-model Analysis of Soil Permeability and Flood Susceptibility Interrelationships

A comparative examination of the permeability map (Figure 13) against each model's flood susceptibility output (Figure 14) reveals a clear spatial relationship between areas of low infiltration capacity and high flood risk [100-102]. In all five correlation maps, zones characterized by lower permeability (classified as low to moderate) overlap consistently with the regions.

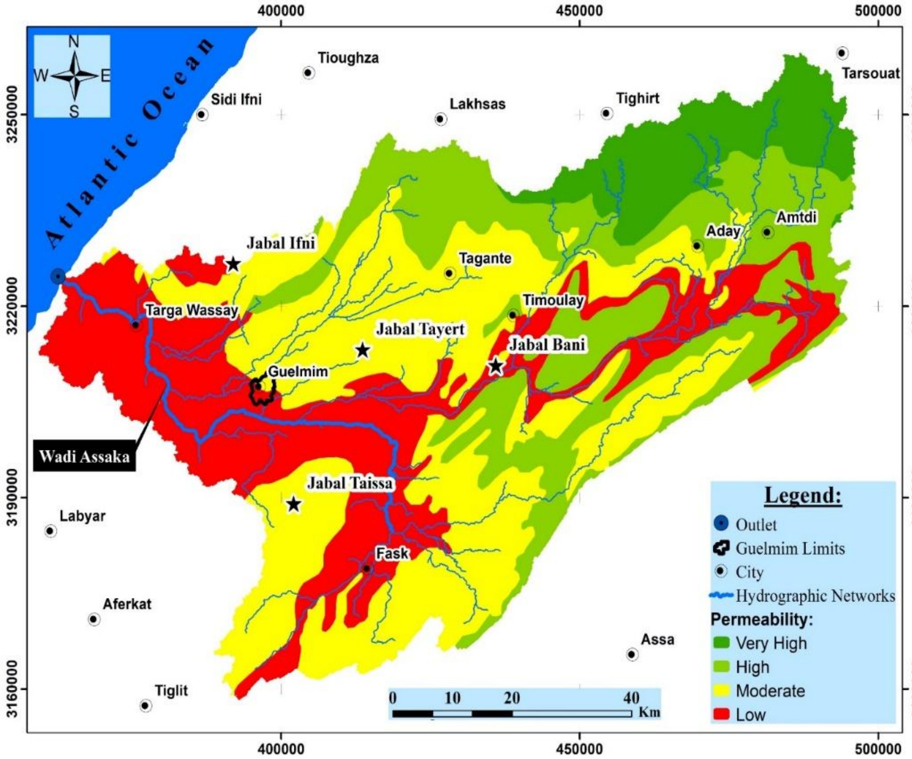

Figure 13. Spatial distribution of soil permeability in the study area

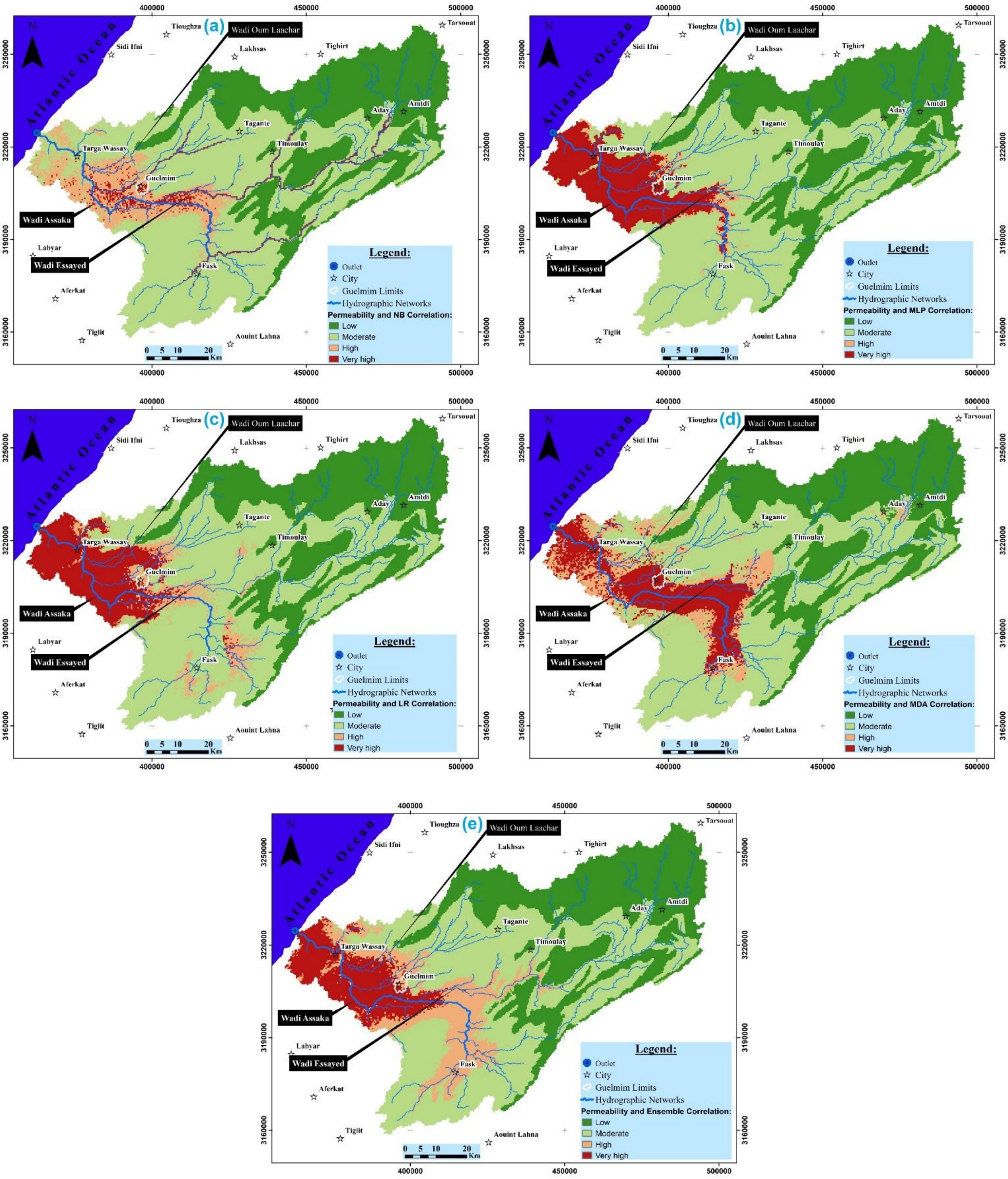

Figure 14. Multi-model correlation analysis of soil permeability and flood susceptibility ((a) naive bayes; (b) logistic regression; (c) multivariate discriminant analysis; (d) multi-layer perceptron; (e) ensemble voting classifier)

identified by the algorithms as highly susceptible to flooding. For instance, the Naive Bayes correlation map (Figure 14-a) highlights that areas in the southwestern portion of the study region where soils are less permeable coincide with elevated flood susceptibility. A similar pattern emerges in the MLP correlation map (Figure 14-b), where the distribution of low-permeability surfaces closely aligns with high-risk flood zones. In the Logistic Regression correlation map (Figure 14-c), moderately permeable zones throughout the central and eastern sections of the area likewise exhibit an appreciable tendency toward flood occurrence.

Meanwhile, the MDA correlation map (Figure 14-d) underscores the relationship between limited infiltration capacity and flood susceptibility, particularly around Wadi Essayed. Finally, the Ensemble correlation map (Figure 14-e) integrates these findings, reinforcing that low-permeability landscapes consistently correspond to higher susceptibility levels. Collectively, these correlations emphasize that soil permeability is a critical determinant of flash flood vulnerability, underscoring the importance of infiltration capacity in effective flood hazard assessment.

According to Figure 4-b and Figure 5, alluvium et recent reg deposits (Upper Proterozoic & Cambrian Lower) typically characterize areas with low flood susceptibility, prominently observed in the northeastern regions. Their high permeability facilitates effective infiltration and significantly reduces surface runoff, making these areas highly suitable for sustainable agricultural practices and safe urban expansion.

Terraces, old alluvial cones, scree, and lacustrine limestone formations (Cambrian Lower, Eocene, Ordovician) predominantly correlate with moderate flood susceptibility areas. These lithologies possess intermediate permeability, allowing partial infiltration but rapidly becoming saturated during intense rainfall, thereby generating potential surface runoff. Spatial analysis confirms their clear association with moderately susceptible flood zones.

Geological formations comprising tuffs, alluvial cones, fractured limestones, and shales (Pleistocene, Silurian, Proterozoic, Ordovician, Cambrian, Eocene) significantly overlap moderate to high susceptibility areas. Although fractures impart partial permeability, they typically facilitate rapid runoff rather than deep infiltration. This condition notably aligns with flood-prone regions in western and central watershed areas, particularly near Wadi Assaka and Wadi Essayed.

Lithologies consisting of limestone, siltstone, dolomite, shale, and sandstone with clay intercalations (Pliocene, Upper Proterozoic, Cambrian, Ordovician, Pleistocene) consistently exhibit high flood susceptibility. Clay-rich layers drastically reduce permeability, promoting rapid runoff during heavy rainfall events. The flood susceptibility maps highlight these geological units in the western-central watershed as critical, indicating an urgent need for targeted flood mitigation measures.

Sandstone and massive quartzite formations (Eocene, Cambrian, Holocene Fluviatile, Pleistocene) strongly correlate with regions classified as very high flood susceptibility, especially around Guelmim city. Their extremely low permeability causes rapid surface runoff, substantially increasing flood hazards, particularly in urbanized regions and near major river channels.

This integrated analysis highlights the clear spatial relationships between lithological characteristics and flood susceptibility, emphasizing the influential role of lithology in flood dynamics within the watershed. Critical zones include sandstone and massive quartzite-dominated areas near Guelmim, requiring immediate flood intervention measures. Moderate to high-risk areas, characterized by fractured limestones, shales, and clay-rich formations, necessitate integrated flood management strategies such as improved drainage systems and strategic land-use planning. Conversely, lower-risk regions dominated by alluvial and recent reg deposits represent safer zones suitable for sustainable urban growth and agricultural development, although continued monitoring is essential to prevent vulnerability escalation.

3.9. Extended Comparison with Previous Studies

The maps and metrics align closely with recent work in the Assaka watershed using expert-based and machine-learning approaches. For example, a comparative AHP vs fuzzy-logic study for Assaka reported that the fuzzy SUM operator mapped ~67% of the basin as high–very high susceptibility, while AHP mapped ~30%, underscoring how method choice and thresholds expand or contract the “high” footprint. Our ensemble (~18.9% high+very high) sits between these extremes, offering a more conservative, operationally focused footprint for prioritizing interventions [4].

Machine-learning applications in and around Assaka echo our factor rankings and spatial hotspots. A Random Forest case study centered on Assaka likewise highlighted corridors along Wadi Essayed and Oum Laachar, with susceptibility reinforced by LST, soil moisture, drainage characteristics, and local geology—converging with our ensemble and MLP interpretations. In other Moroccan basins, ML/ensemble models consistently outperform linear baselines (LR/MDA) in AUC and F1 [9]. For instance, Islam et al. (2021) [103] showed advanced ensembles (Dagging/Random Subspace + ANN) surpassing single models; Pham et al. (2021) [104] likewise improved performance using Bagging/Decorate hybrids; more recently, ensembles in the Houz/High Atlas and other regions reaffirmed superior skill (e.g., RF/XGBoost/stacking) [79]. These findings mirror our results where MLP and the voting ensemble dominate LR/MDA/NB across all metrics [103, 104].

Regarding drivers, prior work repeatedly elevates topography (DEM/TPI) and drainage convergence (flow accumulation, drainage density, SPI), alongside surface conditions (SMI, LST/LULC) and substrate permeability—the same physical controls our jackknife and feature-importance analyses identify. In Assaka’s expert-based mapping, high weights assigned to SMI and drainage metrics sharpened flood belts along the main wadis; our models quantify the same pattern, but with tighter urban-fringe hotspots around Guelmim [4, 14].

Spatially, our ensemble's emphasis on Essayed–Oum Laachar corridors and the Guelmim fringe is consistent with mapped hotspots and with the documented 2014 disaster, when southern Morocco—especially the Guelmim region—suffered substantial losses (national toll ~31–36; ~24 fatalities near Guelmim alone). This historical context validates why our highest classes cluster along valley bottoms and urbanized channels, and why drainage upgrades and land-use control there are critical.

Beyond Assaka, Moroccan ML studies (e.g., Tetouan, Houz plain) using GEE/ANN/RF families also report ANN/ensemble superiority and highlight SMI/LST + DEM/TPI as recurrent predictors—directly consistent with our MLP/ensemble dominance and factor rankings [79, 105].

Why our results differ from some expert-based outputs: (i) criterion weighting & membership functions can inflate high-risk extents (e.g., fuzzy SUM ≈ 67% vs AHP ≈ 30%); (ii) threshold selection for class breaks varies by study; (iii) inventory & sampling and event chronology influence learned decision boundaries (e.g., wetter antecedent conditions favoring SMI). Our ensemble uses out-of-sample validation to balance omission/commission, yielding a compact yet defensible ~19% high-risk footprint that concentrates on corridors already validated by previous studies and historical impacts [4].

4. Conclusions

This study successfully demonstrated the effectiveness of an integrated ensemble modeling approach, utilizing Naive Bayes (NB), Multivariate Discriminant Analysis (MDA), Multilayer Perceptron (MLP), and Logistic Regression (LR), in generating an accurate and robust flash flood susceptibility map for the Assaka watershed in southern Morocco. The ensemble method enhanced predictive accuracy by synthesizing the strengths of individual algorithms, significantly improving reliability in flood risk assessment.

Key insights revealed the critical influence of terrain elevation and configuration, with the Digital Elevation Model (DEM) emerging as the dominant predictor. Other influential variables identified include Land Surface Temperature (LST), Topographic Position Index (TPI), Soil Moisture Index (SMI), and soil type, underscoring their importance within varying modeling contexts. Comparative susceptibility maps highlighted distinct differences among modeling techniques, emphasizing the ensemble method's balanced and comprehensive representation of flood risk. Specifically, susceptibility class distributions varied notably, with Logistic Regression (LR) and Multivariate Discriminant Analysis (MDA) classifying approximately 74% of the area as low susceptibility primarily in the northeastern and eastern regions, and very high susceptibility covering around 12.29% and 12.70%, respectively, mainly in southwestern areas. The Multilayer Perceptron (MLP) model identified the largest low susceptibility area at 83.74% predominantly in northeastern regions, and 13.42% as very high susceptibility largely in the southwestern areas. Naive Bayes (NB) indicated the smallest very high susceptibility at 4.22%, concentrated in southwestern regions, with low susceptibility covering 80.54%, mainly in the north and east. The Ensemble method provided a balanced distribution: low susceptibility (66.34%, predominantly northeast), moderate susceptibility (14.77%, central areas), high susceptibility (8.40%, southwest-central areas), and very high susceptibility (10.50%, southwestern areas).

The spatial correlation between soil permeability and flood susceptibility demonstrated the crucial role of infiltration capacity, reinforcing the direct relationship between geological formations and flood risks. Specifically, alluvium and recent reg deposits (Upper Proterozoic & Lower Cambrian) exhibited low susceptibility due to their high permeability, whereas sandstone and massive quartzite formations (Eocene, Cambrian, Holocene Fluviatile, and Pleistocene) indicated very high susceptibility owing to their low infiltration capacity. Terraces, old alluvial cones, scree, and lacustrine limestone formations (Cambrian Lower, Eocene, and Ordovician) predominantly correlated with moderate susceptibility, possessing intermediate permeability but becoming quickly saturated. Geological formations comprising tuffs, alluvial cones, fractured limestones, and shales (Pleistocene, Silurian, Proterozoic, Ordovician, Cambrian, Eocene) significantly overlapped moderate to high susceptibility areas due to rapid runoff facilitated by fractures. Lithologies consisting of limestone, siltstone, dolomite, shale, and sandstone with clay intercalations (Pliocene, Upper Proterozoic, Cambrian, Ordovician, Pleistocene) consistently exhibited high flood susceptibility because clay-rich layers drastically reduced permeability.

This integrated lithological and modeling analysis effectively identified critical areas around Guelmim city, particularly sandstone and quartzite-dominated regions, highlighting urgent flood management and infrastructure intervention needs. Additionally, moderate- to high-risk zones require integrated flood management strategies involving improved drainage and strategic land-use planning, whereas low-risk alluvial zones are recommended for sustainable urban and agricultural expansion.

The originality of this research lies in its methodological advancement and practical application, addressing significant knowledge gaps in integrated flood modeling within semi-arid regions. The findings and developed methodology contribute valuable insights for global flood risk mitigation, informed urban planning, and resilience enhancement, providing a robust and replicable framework for future studies in similarly vulnerable areas.

5. Declarations

5.1. Author Contributions

Conceptualization, S.T., A.Ak., and A.Ar.; methodology, S.T.; software, S.T. and A.Aa.; validation, S.T. and A.Ak.; formal analysis, S.T.; investigation, S.T.; resources, S.T., S.Am., and B.B.; data curation, S.T.; writing—original draft preparation, S.T.; writing—review and editing, S.T. and A.Ak.; visualization, S.T.; supervision, A.Ak.; project administration, A.Ak. All authors have read and agreed to the published version of the manuscript.

5.2. Data Availability Statement

The data presented in this study are available on request from the corresponding author.

5.3. Funding

The authors received no financial support for the research, authorship, and/or publication of this article.

5.4. Acknowledgments

I am likewise indebted to my supervisor, all professors, friends, colleagues, and family members who walked beside me throughout this journey; their steady kindness, encouragement, and faith in my abilities have remained an unfailing source of strength.

5.5. Conflicts of Interest

The authors declare no conflict of interest.

6. References

[1] Aljazeera. (2014). Morocco flash floods leave dozens dead. Available online: https://Aljazeera.Com/News/2014/11/24/Morocco-Flash-Floods-Leave-Dozens-Dead#:~:Text=Boulid%20told%20Al%20Jazeera%20that,But%20chose%20to%20ignore%20them (accessed on November 2025).

[2] Cherif, M., Díaz-Cassou, J., & Megevand, C. (2023). Climate Change and Development in Morocco. Morocco's Quest for Stronger and Inclusive Growth, 121.

[3] FloodList (2014). Death Toll Rises to 32 in Morocco Floods. Available online: https://Floodlist.Com/Africa/Death-Toll-Rises-32-Morocco-Floods#:~:Text=The%20worst%20hit%20area%20is,Are%20still%20a%20major%20concern (accessed on July 2025).

[4] Khaddari, A., Jari, A., Chakiri, S., El Hadi, H., Labriki, A., Hajaj, S., El Harti, A., Goumghar, L., & Abioui, M. (2023). A Comparative Analysis of Analytical Hierarchy Process and Fuzzy Logic Modeling in Flood Susceptibility Mapping in the Assaka Watershed, Morocco. Journal of Ecological Engineering, 24(8), 62–83. doi:10.12911/22998993/165958.

[5] Khalaf, M., Alaskar, H., Hussain, A. J., Baker, T., Maamar, Z., Buyya, R., Liatsis, P., Khan, W., Tawfik, H., & Al-Jumeily, D. (2020). IoT-Enabled Flood Severity Prediction via Ensemble Machine Learning Models. IEEE Access, 8, 70375–70386. doi:10.1109/access.2020.2986090.

[6] Razali, N., Ismail, S., & Mustapha, A. (2020). Machine learning approach for flood risks prediction. IAES International Journal of Artificial Intelligence (IJ-AI), 9(1), 73. doi:10.11591/ijai.v9.i1.pp73-80.

[7] El-Haddad, B. A., Youssef, A. M., Pourghasemi, H. R., Pradhan, B., El-Shater, A.-H., & El-Khashab, M. H. (2020). Flood susceptibility prediction using four machine learning techniques and comparison of their performance at Wadi Qena Basin, Egypt. Natural Hazards, 105(1), 83–114. doi:10.1007/s11069-020-04296-y.

[8] Singha, C., Swain, K. C., Meliho, M., Abdo, H. G., Almohamad, H., & Al-Mutiry, M. (2022). Spatial Analysis of Flood Hazard Zoning Map Using Novel Hybrid Machine Learning Technique in Assam, India. Remote Sensing, 14(24), 6229. doi:10.3390/rs14246229.

[9] Talha, S., Akhssas, A., Aarab, A., Aabi, A., & Berkat, B. (2025). Enhancing flash flood risk prediction: A case study from the Assaka watershed, Guelmim region, Southwestern Morocco. Ecological Engineering & Environmental Technology, 26(1), 8–28. doi:10.12912/27197050/195227.

[10] Atbir, H. (2020). Opportunités et obstacles de la Ceinture verte de Guelmim, Sud-Ouest Marocain. Cinq Continents 10 (22): 304-319.

[11] City Population. (2024). Guelmim. Available online: https://www.citypopulation.de/en/morocco/guelmimouednoun/guelmim/26101030__guelmim/ (accessed on November 2025).

[12] Support the Guardian. (2014). Morocco hit by floods killing 32 people and leaving hundreds stranded. Available online: https://www.theguardian.com/world/2014/nov/24/morocco-flooding-32-killed-stranded (accessed on November 2025).

[13] Theilen-Willige, B., Charif, A., Ouahidi, A., Chaibi, M., Ougougdal, M., & AitMalek, H. (2015). Flash Floods in the Guelmim Area/Southwest Morocco–Use of Remote Sensing and GIS-Tools for the Detection of Flooding-Prone Areas. Geosciences, 5(2), 203–221. doi:10.3390/geosciences5020203.

[14] Talha, S., Maanan, M., Atika, H., & Rhinane, H. (2019). Prediction of Flash Flood Susceptibility Using Fuzzy Analytical Hierarchy Process (FAHP) Algorithms and GIS: A Study Case of Guelmim Region in Southwestern of Morocco. The International Archives of the Photogrammetry, Remote Sensing and Spatial Information Sciences, XLII-4/W19, 407–414. doi:10.5194/isprs-archives-xlii-4-w19-407-2019.

[15] Atta, H. A. (2023). Seasonal Flooding Impact on Land Surface Temperature (LST) in Response to Vegetation Index Using Spectral Radiance Model in Kirkuk, Iraq. IOP Conference Series: Earth and Environmental Science, 1202(1), 012019. doi:10.1088/1755-1315/1202/1/012019.

[16] El Haou, M., Ourribane, M., Ismaili, M., Krimissa, S., & Namous, M. (2025). Enhancing urban flood hazard assessment: a comparative analysis of frequency ratio and xgboost models for precision risk mapping. Ecological Engineering & Environmental Technology, 26(3), 286–300. doi:10.12912/27197050/200141.

[17] Tehrany, M. S., Jones, S., & Shabani, F. (2019). Identifying the essential flood conditioning factors for flood prone area mapping using machine learning techniques. CATENA, 175, 174–192. doi:10.1016/j.catena.2018.12.011.

[18] Lawford, R. G., Prowse, T. D., Hogg, W. D., Warkentin, A. A., & Pilon, P. J. (1995). Hydrometeorological aspects of flood hazards in Canada. Atmosphere-Ocean, 33(2), 303–328. doi:10.1080/07055900.1995.9649535.

[19] Ulloa-Cedamanos, F., Probst, A., Dos-Santos, V., Camboulive, T., Granouillac, F., & Probst, J.-L. (2021). Stream Hydrochemical Response to Flood Events in a Multi-Lithological Karstic Catchment from the Pyrenees Mountains (SW France). Water, 13(13), 1818. doi:10.3390/w13131818.

[20] Bisht, S., Chaudhry, S., Sharma, S., & Soni, S. (2018). Assessment of flash flood vulnerability zonation through Geospatial technique in high altitude Himalayan watershed, Himachal Pradesh India. Remote Sensing Applications: Society and Environment, 12, 35–47. doi:10.1016/j.rsase.2018.09.001.

[21] Giguet-Covex, C., Arnaud, F., Enters, D., Poulenard, J., Millet, L., Francus, P., David, F., Rey, P.-J., Wilhelm, B., & Delannoy, J.-J. (2012). Frequency and intensity of high-altitude floods over the last 3.5 ka in northwestern French Alps (Lake Anterne). Quaternary Research, 77(1), 12–22. doi:10.1016/j.yqres.2011.11.003.

[22] Maranguit, D., Guillaume, T., & Kuzyakov, Y. (2017). Effects of flooding on phosphorus and iron mobilization in highly weathered soils under different land-use types: Short-term effects and mechanisms. CATENA, 158, 161–170. doi:10.1016/j.catena.2017.06.023.

[23] Basri, H., Syakur, S., Azmeri, A., & Fatimah, E. (2022). Floods and their problems: Land uses and soil types perspectives. IOP Conference Series: Earth and Environmental Science, 951(1), 012111. doi:10.1088/1755-1315/951/1/012111.

[24] Soriano, I. R., Prot, J. C., & Matias, D. M. (2000). Expression of tolerance for *Meloidogyne graminicola* in rice cultivars as affected by soil type and flooding. Journal of Nematology, 32(3), 309.

[25] Rahaman, S. N., & Shermin, N. (2022). Identifying the effect of monsoon floods on vegetation and land surface temperature by using Google Earth Engine. Urban Climate, 43, 101162. doi:10.1016/j.uclim.2022.101162.

[26] Xue, Y., Diallo, I., Li, W., David Neelin, J., Chu, P. C., Vasic, R., Guo, W., Li, Q., Robinson, D. A., Zhu, Y., Fu, C., & Oaida, C. M. (2018). Spring Land Surface and Subsurface Temperature Anomalies and Subsequent Downstream Late Spring-Summer Droughts/Floods in North America and East Asia. Journal of Geophysical Research: Atmospheres, 123(10), 5001–5019. Portico. doi:10.1029/2017jd028246.

[27] Pallard, B., Castellarin, A., & Montanari, A. (2009). A look at the links between drainage density and flood statistics. Hydrology and Earth System Sciences, 13(7), 1019–1029. doi:10.5194/hess-13-1019-2009.

[28] Yang, S.-Y., Chang, C.-H., Hsu, C.-T., & Wu, S.-J. (2022). Variation of uncertainty of drainage density in flood hazard mapping assessment with coupled 1D–2D hydrodynamics model. Natural Hazards, 111(3), 2297-2315. doi:10.1007/s11069-021-05138-1.

[29] Nied, M., Hundecha, Y., & Merz, B. (2013). Flood-initiating catchment conditions: a spatio-temporal analysis of large-scale soil moisture patterns in the Elbe River basin. Hydrology and Earth System Sciences, 17(4), 1401–1414. doi:10.5194/hess-17-1401-2013.

[30] Bannari, A., Rhinane, H., & Bahi, H. (2019). Synergy between SMOS-MIRAS and Landsat-OLI/TIRS Data for Soil Moisture Mapping before, during, and after Flash-Flood Storm in Southwestern Morocco. Topics in Hydrometerology. doi:10.5772/intechopen.79554.

[31] Wu, W., Emerton, R., Duan, Q., Wood, A. W., Wetterhall, F., & Robertson, D. E. (2020). Ensemble flood forecasting: Current status and future opportunities. WIREs Water, 7(3). Portico. doi:10.1002/wat2.1432.

[32] Buttle, J. M., Allen, D. M., Caissie, D., Davison, B., Hayashi, M., Peters, D. L., Pomeroy, J. W., Simonovic, S., St-Hilaire, A., & Whitfield, P. H. (2016). Flood processes in Canada: Regional and special aspects. Canadian Water Resources Journal / Revue Canadienne Des Ressources Hydriques, 41(1–2), 7–30. doi:10.1080/07011784.2015.1131629.

[33] Zope, P. E., Eldho, T. I., & Jothiprakash, V. (2016). Impacts of land use–land cover change and urbanization on flooding: A case study of Oshiwara River Basin in Mumbai, India. CATENA, 145, 142–154. doi:10.1016/j.catena.2016.06.009.

[34] Hasan, M. M., Mondol Nilay, M. S., Jibon, N. H., & Rahman, R. M. (2023). LULC changes to riverine flooding: A case study on the Jamuna River, Bangladesh using the multilayer perceptron model. Results in Engineering, 18, 101079. doi:10.1016/j.rineng.2023.101079.

[35] Adnan, M. S. G., Abdullah, A. Y. M., Dewan, A., & Hall, J. W. (2020). The effects of changing land use and flood hazard on poverty in coastal Bangladesh. Land Use Policy, 99, 104868. doi:10.1016/j.landusepol.2020.104868.

[36] Khaldi, L., El Bilali, A., El Abed, A., Krakauer, N., & El Khanchoufi, A. (2025). Developing an explainable and interpretable machine learning model for flood susceptibility mapping. Ecological Engineering & Environmental Technology, 26(1), 201–215. doi:10.12912/27197050/195845.

[37] Adnan, M. S. G., Talchabhadel, R., Nakagawa, H., & Hall, J. W. (2020). The potential of Tidal River Management for flood alleviation in South Western Bangladesh. Science of The Total Environment, 731, 138747. doi:10.1016/j.scitotenv.2020.138747.

[38] Mind'je, R., Li, L., Amanambu, A. C., Nahayo, L., Nsengiyumva, J. B., Gasirabo, A., & Mindje, M. (2019). Flood susceptibility modeling and hazard perception in Rwanda. International Journal of Disaster Risk Reduction, 38, 101211. doi:10.1016/j.ijdrr.2019.101211.

[39] Paiva, R. C. D., & Lima, S. G. (2024). A Simple Model of Flood Peak Attenuation. Water Resources Research, 60(2). Portico. doi:10.1029/2023wr034692.

[40] Tehrany, M. S., Pradhan, B., & Jebur, M. N. (2013). Spatial prediction of flood susceptible areas using rule based decision tree (DT) and a novel ensemble bivariate and multivariate statistical models in GIS. Journal of Hydrology, 504, 69–79. doi:10.1016/j.jhydrol.2013.09.034.

[41] Calderón, H., Pérez, J. E., Chow, M., & Reyna, J. B. (2020). Índice de Posición Topográfica (TPI) para identificar áreas inundables y zonificación de especies vegetales en un manglar del Pacífico Sur de Nicaragua. Revista Torreón Universitario, 9(26), 124–146. doi:10.5377/torreon.v9i26.10264.

[42] Zhran, M., Ghanem, K., Tariq, A., Alshehri, F., Jin, S., Das, J., Pande, C. B., Pramanik, M., Hasher, F. F. Ben & Mousa, A. (2024). Exploring a GIS-based analytic hierarchy process for spatial flood risk assessment in Egypt: a case study of the Damietta branch. Environmental Sciences Europe, 36(1), 184. doi:10.1186/s12302-024-01001-9.

[43] Costache, R., Arabameri, A., Costache, I., Crăciun, A., & Pham, B. T. (2022). New Machine Learning Ensemble for Flood Susceptibility Estimation. Water Resources Management, 36(12), 4765–4783. doi:10.1007/s11269-022-03276-0.

[44] Gupta, L., & Dixit, J. (2024). Investigating the spatial distribution of flood inundation and landforms using topographic position index (TPI) and geomorphon-based automated landform classification methods. Journal of Earth System Science, 133(3). doi:10.1007/s12040-024-02343-x.

[45] Hasegawa, A., Gusyev, M., & Iwami, Y. (2016). Meteorological Drought and Flood Assessment Using the Comparative SPI Approach in Asia Under Climate Change. Journal of Disaster Research, 11(6), 1082–1090. doi:10.20965/jdr.2016.p1082.

[46] Guerreiro, M. J., Lajinha, T., & Abreu, I. (2007). Flood analysis with the standardized precipitation index (SPI), Revista da Faculdade de Ciênca e Tecnologia Porto, 4: 8-14.

[47] Seiler, R. A., Hayes, M., & Bressan, L. (2002). Using the standardized precipitation index for flood risk monitoring. International Journal of Climatology, 22(11), 1365–1376. Portico. doi:10.1002/joc.799.

[48] Tincu, R., Lazar, G., & Lazar, I. (2018). Modified flash flood potential index in order to estimate areas with predisposition to water accumulation. Open Geosciences, 10(1), 593–606. doi:10.1515/geo-2018-0047.

[49] Vojtek, M., & Vojteková, J. (2019). Flood Susceptibility Mapping on a National Scale in Slovakia Using the Analytical Hierarchy Process. Water, 11(2), 364. doi:10.3390/w11020364.

[50] Kourgialas, N. N., & Karatzas, G. P. (2011). Flood management and a GIS modelling method to assess flood-hazard areas—a case study. Hydrological Sciences Journal, 56(2), 212–225. doi:10.1080/02626667.2011.555836.

[51] Najibi, N., Devineni, N., Lu, M., & Perdigão, R. A. P. (2019). Coupled flow accumulation and atmospheric blocking govern flood duration. Npj Climate and Atmospheric Science, 2(1). doi:10.1038/s41612-019-0076-6.

[52] Langston, A. L., & Temme, A. J. A. M. (2019). Bedrock erosion and changes in bed sediment lithology in response to an extreme flood event: The 2013 Colorado Front Range flood. Geomorphology, 328, 1–14. doi:10.1016/j.geomorph.2018.11.015.

[53] Almikaeel, W., Šoltész, A., Čubanová, L., & Baroková, D. (2024). Hydro-informer: a deep learning model for accurate water level and flood predictions. Natural Hazards, 121(4), 3959–3979. doi:10.1007/s11069-024-06949-8.

[54] Keum, H. J., Han, K. Y., & Kim, H. I. (2020). Real-Time Flood Disaster Prediction System by Applying Machine Learning Technique. KSCE Journal of Civil Engineering, 24(9), 2835–2848. doi:10.1007/s12205-020-1677-7.

[55] Khalaf, M., Hussain, A. J., Al-Jumeily, D., Baker, T., Keight, R., Lisboa, P., Fergus, P., & Al Kafri, A. S. (2018). A Data Science Methodology Based on Machine Learning Algorithms for Flood Severity Prediction. 2018 IEEE Congress on Evolutionary Computation (CEC), 1–8. doi:10.1109/cec.2018.8477904.

[56] Liu, J., Wang, J., Xiong, J., Cheng, W., Sun, H., Yong, Z., & Wang, N. (2021). Hybrid Models Incorporating Bivariate Statistics and Machine Learning Methods for Flash Flood Susceptibility Assessment Based on Remote Sensing Datasets. Remote Sensing, 13(23), 4945. doi:10.3390/rs13234945.

[57] Dodangeh, E., Choubin, B., Eigdir, A. N., Nabipour, N., Panahi, M., Shamshirband, S., & Mosavi, A. (2020). Integrated machine learning methods with resampling algorithms for flood susceptibility prediction. Science of the Total Environment, 705, 135983. doi:10.1016/j.scitotenv.2019.135983.

[58] Sangodoyin, A. O., Akinsolu, M. O., Pillai, P., & Grout, V. (2021). Detection and Classification of DDoS Flooding Attacks on Software-Defined Networks: A Case Study for the Application of Machine Learning. IEEE Access, 9, 122495–122508. doi:10.1109/access.2021.3109490.

[59] Giladi, N., Ben-Haim, Z., Nevo, S., Matias, Y., & Soudry, D. (2021). Physics-aware downsampling with deep learning for scalable flood modeling. Advances in Neural Information Processing Systems, 34, 1378-1389.

[60] Chen, J., Li, Q., Wang, H., & Deng, M. (2019). A Machine Learning Ensemble Approach Based on Random Forest and Radial Basis Function Neural Network for Risk Evaluation of Regional Flood Disaster: A Case Study of the Yangtze River Delta, China. International Journal of Environmental Research and Public Health, 17(1), 49. doi:10.3390/ijerph17010049.

[61] Taromideh, F., Fazloula, R., Choubin, B., Emadi, A., & Berndtsson, R. (2022). Urban Flood-Risk Assessment: Integration of Decision-Making and Machine Learning. Sustainability, 14(8), 4483. doi:10.3390/su14084483.

[62] Aswad, F. M., Kareem, A. N., Khudhur, A. M., Khalaf, B. A., & Mostafa, S. A. (2021). Tree-based machine learning algorithms in the Internet of Things environment for multivariate flood status prediction. Journal of Intelligent Systems, 31(1), 1–14. doi:10.1515/jisys-2021-0179.

[63] Ahmadlou, M., Al‐Fugara, A., Al‐Shabeeb, A. R., Arora, A., Al‐Adamat, R., Pham, Q. B., Al‐Ansari, N., Linh, N. T. T., & Sajedi, H. (2020). Flood susceptibility mapping and assessment using a novel deep learning model combining multilayer perceptron and autoencoder neural networks. Journal of Flood Risk Management, 14(1). doi:10.1111/jfr3.12683.

[64] Andaryani, S., Nourani, V., Haghighi, A. T., & Keesstra, S. (2021). Integration of hard and soft supervised machine learning for flood susceptibility mapping. Journal of Environmental Management, 291, 112731. doi:10.1016/j.jenvman.2021.112731.

[65] Maspo, N.-A., Bin Harun, A. N., Goto, M., Cheros, F., Haron, N. A., & Mohd Nawi, M. N. (2020). Evaluation of Machine Learning approach in flood prediction scenarios and its input parameters: A systematic review. IOP Conference Series: Earth and Environmental Science, 479(1), 012038. doi:10.1088/1755-1315/479/1/012038.

[66] Widiasari, I. R., Nugroho, L. E., & Widyawan. (2017). Deep learning multilayer perceptron (MLP) for flood prediction model using wireless sensor network based hydrology time series data mining. 2017 International Conference on Innovative and Creative Information Technology (ICITech), 1–5. doi:10.1109/innocit.2017.8319150.

[67] Youssef, A. M., Pourghasemi, H. R., Mahdi, A. M., & Matar, S. S. (2022). Flood vulnerability mapping and urban sprawl suitability using FR, LR, and SVM models. Environmental Science and Pollution Research, 30(6), 16081–16105. doi:10.1007/s11356-022-23140-3.

[68] Zhao, G., Pang, B., Xu, Z., Peng, D., & Xu, L. (2019). Assessment of urban flood susceptibility using semi-supervised machine learning model. Science of the Total Environment, 659, 940–949. doi:10.1016/j.scitotenv.2018.12.217.

[69] Irawan, L. Y., Sumarmi, Panoto, D., Nabila, Pradana, I. H., & Darmansyah, A. C. (2021). Combination of machine learning model (LR-FR) for flash flood susceptibility assessment in Dawuan Sub watershed Mojokerto Regency, East Java. IOP Conference Series: Earth and Environmental Science, 739(1), 012017. doi:10.1088/1755-1315/739/1/012017.

[70] Rahman, M., Ningsheng, C., Islam, M. M., Dewan, A., Iqbal, J., Washakh, R. M. A., & Shufeng, T. (2019). Flood Susceptibility Assessment in Bangladesh Using Machine Learning and Multi-criteria Decision Analysis. Earth Systems and Environment, 3(3), 585–601. doi:10.1007/s41748-019-00123-y.

[71] Saravanan, S., & Abijith, D. (2022). Flood susceptibility mapping of Northeast coastal districts of Tamil Nadu India using Multi-source Geospatial data and Machine Learning techniques. Geocarto International, 37(27), 15252–15281. doi:10.1080/10106049.2022.2096702.

[72] Luu, C., Bui, Q. D., Costache, R., Nguyen, L. T., Nguyen, T. T., Van Phong, T., Van Le, H., & Pham, B. T. (2021). Flood-prone area mapping using machine learning techniques: a case study of Quang Binh province, Vietnam. Natural Hazards, 108(3), 3229–3251. doi:10.1007/s11069-021-04821-7.

[73] Mahdizadeh Gharakhanlou, N., & Perez, L. (2022). Spatial Prediction of Current and Future Flood Susceptibility: Examining the Implications of Changing Climates on Flood Susceptibility Using Machine Learning Models. Entropy, 24(11), 1630. doi:10.3390/e24111630.

[74] Jamali, B., Haghighat, E., Ignjatovic, A., Leitão, J. P., & Deletic, A. (2021). Machine learning for accelerating 2D flood models: Potential and challenges. Hydrological Processes, 35(4). doi:10.1002/hyp.14064.

[75] Carreau, J., & Bouvier, C. (2015). Multivariate density model comparison for multi-site flood-risk rainfall in the French Mediterranean area. Stochastic Environmental Research and Risk Assessment, 30(6), 1591–1612. doi:10.1007/s00477-015-1166-6.

[76] Tan, H., Ping, W., Yang, T., Li, S., Liu, A., Zhou, J., Groves, J., & Sun, Z. (2007). The Synthetic Evaluation Model for Analysis of Flooding Hazards. The European Journal of Public Health, 17(2), 206–210. doi:10.1093/eurpub/ckl067.

[77] Sellami, E. M., Maanan, M., & Rhinane, H. (2022). Performance of Machine Learning Algorithms for Mapping and Forecasting of Flash Flood Susceptibility in Tetouan, Morocco. The International Archives of the Photogrammetry, Remote Sensing and Spatial Information Sciences, XLVI-4/W3-2021, 305–313. doi:10.5194/isprs-archives-xlvi-4-w3-2021-305-2022.

[78] Mekkaoui, O., Morarech, M., Bouramtane, T., Barbiero, L., Hamidi, M., Akka, H., & Rengasamy, R. P. M. (2025). Unveiling Urban Flood Vulnerability: A Machine Learning Approach for Mapping High Risk Zones in Tetouan City, Northern Morocco. Urban Science, 9(3), 70. doi:10.3390/urbansci9030070.

[79] Bammou, Y., Benzougagh, B., Igmoullan, B., Ouallali, A., Kader, S., Spalevic, V., Sestras, P., Billi, P., & Marković, S. B. (2024). Optimizing flood susceptibility assessment in semi-arid regions using ensemble algorithms: a case study of Moroccan High Atlas. Natural Hazards, 120(8), 7787–7816. doi:10.1007/s11069-024-06550-z.

[80] Janizadeh, S., Avand, M., Jaafari, A., Phong, T. V., Bayat, M., Ahmadisharaf, E., Prakash, I., Pham, B. T., & Lee, S. (2019). Prediction Success of Machine Learning Methods for Flash Flood Susceptibility Mapping in the Tafresh Watershed, Iran. Sustainability, 11(19), 5426. doi:10.3390/su11195426.

[81] Al-Kindi, K. M., & Alabri, Z. (2024). Investigating the Role of the Key Conditioning Factors in Flood Susceptibility Mapping Through Machine Learning Approaches. Earth Systems and Environment, 8(1), 63–81. doi:10.1007/s41748-023-00369-7.

[82] He, F., Liu, S., Mo, X., & Wang, Z. (2025). Interpretable flash flood susceptibility mapping in Yarlung Tsangpo River Basin using H2O Auto-ML. Scientific Reports, 15(1). doi:10.1038/s41598-024-84655-y.

[83] Islam, T., Zeleke, E. B., Afroz, M., & Melesse, A. M. (2025). A Systematic Review of Urban Flood Susceptibility Mapping: Remote Sensing, Machine Learning, and Other Modeling Approaches. Remote Sensing, 17(3), 524. doi:10.3390/rs17030524.

[84] Narimani, R., Jun, C., Shahzad, S., Oh, J., & Park, K. (2021). Application of a Novel Hybrid Method for Flood Susceptibility Mapping with Satellite Images: A Case Study of Seoul, Korea. Remote Sensing, 13(14), 2786. doi:10.3390/rs13142786.

[85] Ogato, G. S., Bantider, A., Abebe, K., & Geneletti, D. (2020). Geographic information system (GIS)-Based multicriteria analysis of flooding hazard and risk in Ambo Town and its watershed, West shoa zone, oromia regional State, Ethiopia. Journal of Hydrology: Regional Studies, 27, 100659. doi:10.1016/j.ejrh.2019.100659.

[86] Negese, A., Worku, D., Shitaye, A., & Getnet, H. (2022). Potential flood-prone area identification and mapping using GIS-based multi-criteria decision-making and analytical hierarchy process in Dega Damot district, northwestern Ethiopia. Applied Water Science, 12(12). doi:10.1007/s13201-022-01772-7.

[87] Roohi, M., Dehghani, J., Irani, M., & Mina, P. (2025). A comprehensive review of flood damage in mountainous regions: challenges, solutions, and advanced management technologies. Discover Geoscience, 3(1). doi:10.1007/s44288-025-00145-2.

[88] Ogden, F. L., Raj Pradhan, N., Downer, C. W., & Zahner, J. A. (2011). Relative importance of impervious area, drainage density, width function, and subsurface storm drainage on flood runoff from an urbanized catchment. Water Resources Research, 47(12). doi:10.1029/2011wr010550.

[89] Corapci, F., & Ozdemir, H. (2024). A new approach to flood susceptibility analysis of urbanised alluvial fans: the case of Bursa City (Türkiye). Natural Hazards, 120(14), 12909–12932. doi:10.1007/s11069-024-06723-w.

[90] Li, K., Guo, L., Wang, G., Gao, J., Ma, J., Li, J., Huang, P., Zhai, B., & Sun, X. (2025). A novel hybrid framework of high-resolution flood susceptibility mapping in ungauged mountainous regions. Weather and Climate Extremes, 50, 100822. doi:10.1016/j.wace.2025.100822

[91] Manopkawee, P., Mankhemthong, N., Kanthata, S., & Sooksabai, C. (2025). Quantifying Regional-Scale Flash Flood Susceptibility Using Watershed Geomorphometry-Based Approach along the High Range, West of Chiang Mai Basin, Northern Thailand. Natural Hazards Research. doi:10.1016/j.nhres.2025.07.001.

[92] Aichi, A., Ikirri, M., Ait Haddou, M., Quesada-Román, A., Sahoo, S., Singha, C., Sajinkumar, K. S., & Abioui, M. (2024). Integrated GIS and analytic hierarchy process for flood risk assessment in the Dades Wadi watershed (Central High Atlas, Morocco). Results in Earth Sciences, 2, 100019. doi:10.1016/j.rines.2024.100019.

[93] Ghosh, B., Garg, S. & Motagh, M. (2022). Automatic flood detection from sentinel-1 data using deep learning architectures. ISPRS Annals of the Photogrammetry, Remote Sensing and Spatial Information Sciences, 5(3), 201–208. doi:10.5194/isprs-Annals-V-3-2022-201-2022.

[94] Purwati, S. E., & Pristyanto, Y. (2024). Model Random Forest and Support Vector Machine for Flood Classification in Indonesia. Sinkron, 8(4), 2261–2268. doi:10.33395/sinkron.v8i4.13973.

[95] Jiang, S., Zheng, Y., Wang, C., & Babovic, V. (2022). Uncovering Flooding Mechanisms Across the Contiguous United States Through Interpretive Deep Learning on Representative Catchments. Water Resources Research, 58(1). doi:10.1029/2021wr030185.

[96] Patil, K. R., Doi, T., & Behera, S. K. (2023). Predicting extreme floods and droughts in East Africa using a deep learning approach. npj Climate and Atmospheric Science, 6(1). doi:10.1038/s41612-023-00435-x.

[97] Wang, X., Bai, Y., Zhang, L., Jiang, G., Zhang, P., Liu, J., Li, L., Huang, L., & Qin, P. (2024). Identification and core gene-mining of Weighted Gene Co-expression Network Analysis-based co-expression modules related to flood resistance in quinoa seedlings. BMC Genomics, 25(1). doi:10.1186/s12864-024-10638-y.

[98] Liu, Z., Felton, T., & Mostafavi, A. (2024). Interpretable machine learning for predicting urban flash flood hotspots using intertwined land and built-environment features. Computers, Environment and Urban Systems, 110, 102096. doi:10.1016/j.compenvurbsys.2024.102096.

[99] Yuan, F., Yang, Y., Li, Q., & Mostafavi, A. (2022). Unraveling the Temporal Importance of Community-Scale Human Activity Features for Rapid Assessment of Flood Impacts. IEEE Access, 10, 1138–1150. doi:10.1109/access.2021.3137651.

[100] DiStasi, M. R., & Ley, K. (2009). Opening the flood-gates: how neutrophil-endothelial interactions regulate permeability. Trends in Immunology, 30(11), 547–556. doi:10.1016/j.it.2009.07.012.

[101] Hu, M., Zhang, X., Siu, Y., Li, Y., Tanaka, K., Yang, H., & Xu, Y. (2018). Flood Mitigation by Permeable Pavements in Chinese Sponge City Construction. Water, 10(2), 172. doi:10.3390/w10020172.

[102] Warhurst, J. R., Parks, K. E., McCulloch, L., & Hudson, M. D. (2014). Front gardens to car parks: Changes in garden permeability and effects on flood regulation. Science of The Total Environment, 485–486, 329–339. doi:10.1016/j.scitotenv.2014.03.035.

[103] Towfiqul Islam, A. R. M., Talukdar, S., Mahato, S., Kundu, S., Eibek, K. U., Pham, Q. B., Kuriqi, A., & Linh, N. T. T. (2021). Flood susceptibility modelling using advanced ensemble machine learning models. Geoscience Frontiers, 12(3), 101075. doi:10.1016/j.gsf.2020.09.006.

[104] Pham, B. T., Jaafari, A., Phong, T. V., Yen, H. P. H., Tuyen, T. T., Luong, V. V., Nguyen, H. D., Le, H. V., & Foong, L. K. (2021). Improved flood susceptibility mapping using a best first decision tree integrated with ensemble learning techniques. Geoscience Frontiers, 12(3), 101105. doi:10.1016/j.gsf.2020.11.003.

[105] Sellami, E. M., & Rhinane, H. (2024). Google Earth Engine and Machine Learning for Flash Flood Exposure Mapping—Case Study: Tetouan, Morocco. Geosciences, 14(6), 152. doi:10.3390/geosciences14060152.